RESEARCH ARTICLE | JULY 09 2024

Benchmarking various nonadiabatic semiclassical mapping dynamics methods with tensor-train thermo-field dynamics ⊘
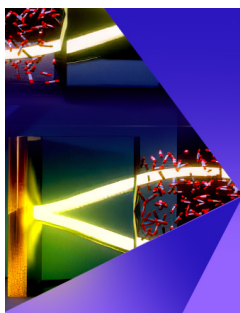
Zengkui Liu [iD] ; Ningyi Lyu [iD] ; Zhubin Hu [iD] ; Hao Zeng [iD] ; Victor S. Batista [iD] ; Xiang Sun [✉] [iD]

Check for updates

View Online   Export Citation

Benchmarking various nonadiabatic semiclassical mapping dynamics methods with tensor-train thermo-field dynamics

Zengkui Liu,[1,2,3] (ID) Ningyi Lyu,[1,4] (ID) Zhubin Hu,[1,2,5] (ID) Hao Zeng,[1,2,5] (ID) Victor S. Batista,[4] (ID)
and Xiang Sun[1,2,3,5,a)] (ID)

AFFILIATIONS

[1] Division of Arts and Sciences, NYU Shanghai, 567 West Yangsi Road, Shanghai 200124, China
[2] NYU-ECNU Center for Computational Chemistry at NYU Shanghai, 3663 Zhongshan Road North, Shanghai 200062, China
[3] Department of Chemistry, New York University, New York, New York 10003, USA
[4] Department of Chemistry, Yale University, P.O. Box 208107, New Haven, Connecticut 06520-8107, USA
[5] State Key Laboratory of Precision Spectroscopy, East China Normal University, Shanghai 200062, China

[a)] Author to whom correspondence should be addressed: xiang.sun@nyu.edu

ABSTRACT

Accurate quantum dynamics simulations of nonadiabatic processes are important for studies of electron transfer, energy transfer, and photochemical reactions in complex systems. In this comparative study, we benchmark various approximate nonadiabatic dynamics methods with mapping variables against numerically exact calculations based on the tensor-train (TT) representation of high-dimensional arrays, including TT-KSL for zero-temperature dynamics and TT-thermofield dynamics for finite-temperature dynamics. The approximate nonadiabatic dynamics methods investigated include mixed quantum–classical Ehrenfest mean-field and fewest-switches surface hopping, linearized semiclassical mapping dynamics, symmetrized quasiclassical dynamics, the spin-mapping method, and extended classical mapping models. Different model systems were evaluated, including the spin-boson model for nonadiabatic dynamics in the condensed phase, the linear vibronic coupling model for electronic transition through conical intersections, the photoisomerization model of retinal, and Tully's one-dimensional scattering models. Our calculations show that the optimal choice of approximate dynamical method is system-specific, and the accuracy is sensitively dependent on the zero-point-energy parameter and the initial sampling strategy for the mapping variables.

Published under an exclusive license by AIP Publishing. https://doi.org/10.1063/5.0208708

I. INTRODUCTION

Quantum dynamics simulation of nonadiabatic processes in complex systems is vital to the understanding of many photoinduced chemical reactions[1–10] as well as charge and energy transfer processes in solar energy conversion materials and photosynthesis.[11–16] While directly integrating the time-dependent Schrödinger equation (TDSE) offers the most accurate and detailed results, this approach is not practical for the simulation of complicated molecular systems due to the computational cost that grows exponentially with the number of degrees of freedom (DOF). The various computational approaches developed to circumvent the exponential scaling problems and enable the simulation of nonadiabatic dynamics in condensed phases can be roughly sorted into two categories: those that involve physical approximations and those that do not. Methods that do not involve physical approximation, henceforth referred to as the "numerically exact" methods, integrate the TDSE or the quantum Liouville equation (QLE) with cost-effective numerical techniques that converge to the true answer with increased computational investment.[3,17–22] For instance, techniques based on tensor networks[3,20,23–25] or the Feynman–Vernon influence functional[21,22,26–31] have been extensively utilized to study molecular systems. Despite their accuracy upon convergence, numerically exact methods are, in general, still quite expensive and are typically restricted to systems with a few tens to a few hundreds of DOF.

On the other hand, the approximate methods[2,32–35] reduce the computational cost by invoking a classical-like trajectory description for part of the system, most typically the nuclear DOF, and are often able to treat systems with 10^3–10^5 DOF.[36–42] These methods range from traditional mixed quantum–classical (MQC) methods, such as mean-field Ehrenfest and fewest-switches surface hopping (FSSH) methods, to a variety of nonadiabatic semiclassical dynamics. While approximate methods simulate the time-evolution of significantly more complicated systems, the accuracy for the description of quantum motion with classical trajectories remains an open question, and the answer might not only differ by the specific approximate methods but also depend on the characters of the simulated system, such as the shape of the potential energy surfaces (PESs), the type of electronic couplings, and the simulated temperature.

Recently, a family of nonadiabatic semiclassical dynamical methods with the mapping Hamiltonian has emerged, which provides a balanced performance in accuracy and computational efficiency. The Meyer–Miller Stock–Thoss (MMST) mapping Hamiltonian[32,34] provides a mapping between F discrete electronic states and a collection of F singly excited harmonic oscillators as a generalization of Schwinger's bosonization,[43,44] where the positions and momenta of these oscillators serve as Cartesian mapping variables for further trajectory-based semiclassical approximations. For example, the linearized semiclassical (LSC) dynamics can be derived by performing linearization approximation to the full semiclassical initial value representation (SC-IVR) as shown by Miller and co-workers, and the LSC method refrains from evaluating the computationally expensive stability matrix as required by SC-IVR.[35,45] An alternative way of arriving at LSC shown by Shi and Geva is to linearize the forward–backward action in the real-time path-integral formulation[46] and thus can also be called the linearized path integral approach.[47–49] It is noted that the LSC expression for the time correlation function is identical to the expression obtained from the classical Wigner approach, featuring Wigner transformation of nuclear density used for the initial sampling of nuclear DOF.[46] The LSC strategy was demonstrated in many condensed-phase systems to be effective in capturing the important quantum effects, for example, in the processes involving electronic transition and vibrational relaxation.[46,50] It can be shown that combining the quantum–classical Liouville equation (QCLE) with the mapping Hamiltonian generates the Poisson-bracket mapping equation (PBME) approximation, which is another version of the semiclassical mapping dynamics.[51] Recently, Saller *et al.*[42] and Gao *et al.*[52] have demonstrated that the LSC mapping dynamics can be combined with the resolution of identity operator to have better population dynamics in model systems.

The symmetrical quasiclassical (SQC) method proposed by Cotton and Miller[37] is also based on the MMST mapping Hamiltonian, but it utilizes a windowing approach for determining the electronic population. The idea of the SQC method originated from the Bohr–Sommerfeld quantization, where quantum states are associated with integer values of action variables.[53] In SQC dynamics, the positions and momenta mapping variables of the electronic DOF are transformed into the action–angle (a–a) variables, which evolve together with the nuclear DOF classically. The electronic population is obtained by filtering the action variables with a finite-width symmetrical window function, approximating the delta function. The square window function[53] serves as a coarse-grained filter for quantizing the populations of different electronic states, whose ensemble average over many trajectories provides continuous evolution of the electronic populations. The width of the window function is controlled by the zero-point energy (ZPE) parameter γ (the full quantum $\gamma = 0.5$), whose value can be fixed such as $\gamma = (\sqrt{3} - 1)/2 \approx 0.366$ or adjusted on a per-trajectory basis such that the initial nuclear forces correspond to the potential energy surface (PES) of the initial electronic state.[54] Recently, the triangle window function (with optimal $\gamma = 1/3$) has been reported to give superior nonadiabatic dynamics than the original square window function for the weak coupling case.[38] SQC dynamics can also be applied to the spin-mapping Hamiltonian as proposed by Cotton and Miller,[55] where each electronic state is represented as a spin-1/2 DOF with spin-up and spin-down corresponding to the occupied and unoccupied states, and the creation and annihilation operators of electronic state are represented as the angular momentum ladder operators.

There are other mapping strategies for representing discrete electronic states, for instance, using a spin-S (such that $2S + 1 = F$) to represent an F-level system was suggested by Meyer and Miller in 1979.[56] Recently, a general spin-mapping (SPM) approach has been proposed by Runeson and Richardson in 2019, which was formulated by using the Stratonovich–Weyl transform for a spin-1/2 for the two-level system[40] and a generalized F-level system that preserves the $SU(F)$ symmetry.[41,57,58] Using the P, Q, and W representations of the Stratonovich–Weyl transform for the spin operators, the corresponding SPM approaches require specific ZPE parameters and hypersphere radius for the full-sphere sampling of the mapping variables and the W scheme is the recommended version of SPM.[41] As it turns out, the P, Q, and W schemes of SPM are equivalent to a special set of ZPE parameter choices in the extended classical mapping models (eCMMs) proposed by He and Liu in 2019, which are based on the Wigner–Weyl transform of the phase-space representation of quantum mechanics and a constraint sphere for the initial mapping phase-space variables, and the resulting ZPE parameters can be any values in $\gamma \in (-1/F, \infty)$.[59] It is noted that s may give accurate population dynamics for some systems when the ZPE parameter takes a negative value, such as $\gamma = -0.2$. The SPM/eCMM approaches are based on the initial sampling of the mapping variables on the full-sphere that reinforce the total population to be unity, but in some cases, the initial nuclear forces might cause unphysical nuclear dynamics due to the uniform sampling of all electronic states and thus their PESs.[14] To circumvent this issue, techniques ensuring the initial effective forces to be evaluated on the initial state's PES are developed like adjusting ZPE per trajectory by auxiliary commutator variables for eCMM[60] or focused mapping variable sampling for SPM.[41] However, the ZPE adjusting might not fully resolve the inverted potential issue for the mapping dynamics.[54] It is important to mark that the equations of motion for these spin-mapping approaches can be formulated to be the same in terms of Cartesian mapping variables as those for the LSC mapping dynamics defined in the MMST Hamiltonian, and the major differences between these mapping dynamics are the ZPE parameter, initial sampling, and observable evaluation.[33,34,61] In addition, the spin-mapping and phase-space-mapping strategies solve the problem of MMST mapping variables deviating from the singly excited oscillator (SEO) subspace, hence giving a better description of the identity operator and thus population dynamics. Although these

mapping relations would be exact for the electronic dynamics in the frozen-nuclei limit,[62] their accuracy has to be tested when applied to trajectory-based nonadiabatic dynamics with classical nuclear DOF since the coupled electronic-nuclear dynamics would be approximate. A detailed test on these different mapping dynamics as well as mixed quantum–classical dynamics is lacking, especially with more challenging models, ranging from spin-boson models to systems with anharmonic potentials and non-Condon electronic couplings.

To this end, we report a benchmark study for various approximate nonadiabatic mapping dynamics against the numerically exact quantum dynamics provided by tensor-train (TT) based methods. The tensor-train format for high-dimensional tensors provides a practical way for evolving the wavepacket of quantum systems with high-dimensional nuclear and electronic DOF, mitigating the exponential scaling problem, the so-called curse of dimensionality. In the TT format or the matrix product state (MPS), an Nth order wavefunction tensor can be approximated as a chain of N core tensors of order up to 3, and each core tensor corresponds to one physical dimension. A traditional split-operator Fourier transform (SOFT) method for wavepacket dynamics utilizes the Trotter expansion of the time-evolution operator and avoids implementing the nonlocal kinetic energy operator in the position space by Fourier transforming to the momentum space for kinetic energy propagation, but SOFT can handle very few DOF. Combining the TT format and SOFT propagation method, Greene and Batista proposed the tensor-train split-operator Fourier transform (TT-SOFT) method for direct nonadiabatic wavepacket propagation in high-dimensional systems.[3] In TT-SOFT, the propagation involves the scaling and squaring that generate high-rank TT, and then, the rounding operation gives the low-rank approximation, but it may cause unstable norm conservation when used with limited rank. A more efficient way to propagate quantum dynamics is the TT implementation of the dynamical low-rank approximation, called the TT-KSL method[20,63] or the time-dependent variational principle (TDVP) with projector splitting,[25,64–66] which stays in the fixed rank manifold by using projection onto the tangent space, giving rise to an optimal and efficient solution of propagation in the low-rank subspace. Recently, Lyu *et al.* have proposed tensor-train split-operator KSL (TT-SOKSL)[20] that takes advantage of the efficient propagation of TT-KSL on the low-rank manifold and also the local kinetic energy operator that only requires vector–vector multiplications in the momentum space as in SOFT. TT-SOKSL was shown to give better norm conservation than TT-SOFT in a 25-dimensional anharmonic and non-Condon model of retinal photoisomerization.[20] Solving the TDSE using the above-mentioned TT-based methods could only provide wavepacket dynamics at zero temperature, and thermofield dynamics (TFD) provides a way for solving the thermal Schrödinger equation that describes the thermal wavepacket defined in the double space. The combination of TT and TFD would allow for quantum dynamical treatment for multi-dimensional systems, and in particular, for harmonic systems, thermal Bogoliubov transformation enables an analytical expression for the thermal state in TT-TFD.[67] In addition, TT-TFD has been applied to compute finite-temperature quantum dynamics of spin-boson models and the Fenna–Matthews–Olson (FMO) complex[68] as well as the kernels in the Nakajima–Zwanzig generalized quantum master equation.[69]

In this work, we aim to test a broad range of models with qualitatively contrasting features (i.e., harmonic vs anharmonic PESs, Condon vs non-Condon electronic coupling, and zero temperature vs finite temperature) as well as quantitatively different sets of parameters (i.e., strong vs weak reorganization energies and biased vs unbiased electronic gap) to facilitate a comprehensive comparison among different application scenarios. We envision this work to provide practical recommendations for the choice of approximate mapping dynamics methods in simulating nonadiabatic dynamics in complex systems.

The rest of this paper is organized as follows. Section II gives an overview of all approximate and numerically exact methods employed in this work. Section III presents the benchmarked models. Section IV describes the simulation details. Section V reports and discusses the results. Section VI provides the concluding remarks.

II. THEORY

A. Various semiclassical and quasiclassical mapping dynamics

We summarize the semiclassical and quasiclassical mapping dynamical methods that will be benchmarked. Consider a general multi-state system with F electronic states and N total nuclear DOF, whose total Hamiltonian in the diabatic basis is written as

$$\hat{H} = \frac{\hat{\mathbf{P}}^2}{2} + \sum_{j,k}^{F} V_{jk}(\hat{\mathbf{R}})|j\rangle\langle k| = \frac{\hat{\mathbf{P}}^2}{2} + \hat{V}(\hat{\mathbf{R}}), \tag{1}$$

where $\hat{\mathbf{P}} = (\hat{\mathbf{P}}_1, \ldots, \hat{\mathbf{P}}_N)$ and $\hat{\mathbf{R}} = (\hat{\mathbf{R}}_1, \ldots, \hat{\mathbf{R}}_N)$ denote the N mass-weighted nuclear coordinates and momenta; $|j\rangle$ $(j = 1, \ldots, F)$ represent the jth electronic state; $V_{jj}(\hat{\mathbf{R}}) \equiv V_j(\hat{\mathbf{R}})$ is the PES of the jth electronic state; $V_{jk}(\hat{\mathbf{R}})$ is the electronic coupling between the jth and the kth electronic states $(j \neq k)$; and $\hat{V}(\hat{\mathbf{R}}) = \sum_{j,k}^{F} V_{jk}(\hat{\mathbf{R}})|j\rangle\langle k|$ is the electronic Hamiltonian. Within the Condon approximation, $V_{jk}(\hat{\mathbf{R}})$ becomes constant $V_{jk} = \Gamma_{jk}$ $(j \neq k)$ and $V_{jk} = V_{kj}$. The MMST mapping Hamiltonian is based on the mapping from the multi-state electronic Hilbert space to a collection of SEOs,[33,34]

$$|j\rangle \longmapsto \underbrace{|0_1 \cdots 1_j \cdots 0_F\rangle}_{F-\text{states}} \equiv |1_j\rangle, \tag{2}$$

where only the jth oscillator is on its first excited state, while others are on the ground state. The electronic operators $|k\rangle\langle j| \equiv \hat{M}_{kj}$ are mapped to $\hat{a}_k^\dagger \hat{a}_j$ such that the commutator relation $[\hat{a}_j, \hat{a}_k^\dagger] = \delta_{kj}$ is satisfied, where $\hat{a}_k^\dagger$ and $\hat{a}_j$ are the creation and annihilation operators of quantum oscillators. The quantum-mechanically exact mapping is given by

$$|j\rangle\langle j| \longmapsto \hat{a}_j^\dagger \hat{a}_j = \frac{1}{2\hbar}(\hat{q}_j^2 + \hat{p}_j^2) - \frac{1}{2},$$
$$|k\rangle\langle j| \longmapsto \hat{a}_k^\dagger \hat{a}_j = \frac{1}{2\hbar}(\hat{q}_k - i\hat{p}_k)(\hat{q}_j + i\hat{p}_j). \tag{3}$$

Here, we used that $\hat{a}_j^\dagger = \frac{1}{\sqrt{2\hbar}}(\hat{q}_j - i\hat{p}_j)$, $\hat{a}_j = \frac{1}{\sqrt{2\hbar}}(\hat{q}_j + i\hat{p}_j)$, and $[\hat{q}_j, \hat{p}_k] = i\hbar\delta_{jk}$, where $\hat{q}_j$ and $\hat{p}_j$ are the coordinate and momentum operators of quantum oscillators. Then, taking a classical limit, we

obtain $|j\rangle\langle j| = \frac{1}{2\hbar}(q_j^2 + p_j^2) - \gamma$ and $|k\rangle\langle j| = \frac{1}{2\hbar}(q_k - ip_k)(q_j + ip_j)$, where γ is the zero point energy (ZPE) parameter (when $\gamma = 1/2$ full quantum ZPE is included). Inserting the above relation into Eq. (1), we have the MMST mapping Hamiltonian,

$$H(\mathbf{R}, \mathbf{P}, \mathbf{q}, \mathbf{p}) = \frac{\mathbf{P}^2}{2} + \sum_j^F V_j(\mathbf{R})\left(\frac{1}{2\hbar}q_j^2 + \frac{1}{2\hbar}p_j^2 - \gamma\right)$$
$$+ \sum_{j \neq k}^F V_{jk}(\mathbf{R})\frac{1}{2\hbar}(q_j - ip_j)(q_k + ip_k). \quad (4)$$

Alternatively, it can be equivalently expressed in terms of the symmetrized version,[37,70]

$$H(\mathbf{R}, \mathbf{P}, \mathbf{q}, \mathbf{p}) = \frac{\mathbf{P}^2}{2} + \overline{V}(\mathbf{R}) + \frac{1}{2\hbar}\sum_j^F \left[V_j(\mathbf{R}) - \overline{V}(\mathbf{R})\right](q_j^2 + p_j^2)$$
$$+ \frac{1}{2\hbar}\sum_{j \neq k}^F V_{jk}(\mathbf{R})(q_j - ip_j)(q_k + ip_k), \quad (5)$$

where $\overline{V}(\mathbf{R}) = \frac{1}{F}\sum_j^F V_j(\mathbf{R})$ is the average potential energy. The equations of motion for the semiclassical mapping dynamics are the corresponding Hamilton's equations. The integrator for the mapping Hamiltonian is described in Ref. 71. It is noted that other integrators are also available.[72–75]

In nonadiabatic dynamics, the electronic reduced density matrix (RDM) is a key property, which is defined as $\hat{\sigma}(t) = \text{Tr}_N[\hat{\rho}(t)] = \sum_{j,k}^F \sigma_{jk}(t)|j\rangle\langle k|$, where $\hat{\rho}(t)$ is the overall density matrix and the diagonal $\sigma_{jj}(t)$ and off-diagonal $\sigma_{jk}(t)$ $(j \neq k)$ elements correspond to the electronic population and the electronic coherence, respectively. $\text{Tr}_N[\cdot]$ and $\text{Tr}_e[\cdot]$ stand for the trace over the nuclear and electronic Hilbert spaces, respectively. In a typical nonadiabatic process, the initial state is assumed to be $\hat{\rho}(0) = \hat{\rho}_N(0) \otimes \hat{\sigma}(0) = \sum_{j,k}^F \hat{\rho}_N(0)\sigma_{jk}(0)|j\rangle\langle k|$, where the initial nuclear density is given by $\hat{\rho}_N(0) = \text{Tr}_e[\hat{\rho}(0)]$ and the initial electronic state is a population, for example, $\hat{\sigma}(0) = |m\rangle\langle m|$. The RDM at time t is given by[52]

$$\sigma_{jk}(t) = \sum_{m,n}^F \sigma_{mn}(0)\text{Tr}_N\text{Tr}_e\left[\hat{\rho}_N(0)|m\rangle\langle n|e^{i\hat{H}t/\hbar}|k\rangle\langle j|e^{-i\hat{H}t/\hbar}\right]$$
$$\equiv \sum_{m,n}^F \sigma_{mn}(0)C_{\hat{M}_{mn}\hat{M}_{kj}}(t), \quad (6)$$

where the quantum time correlation function has the form $C_{\hat{A}\hat{B}}(t) = \text{Tr}\left[\hat{\rho}_N(0)\hat{A}e^{i\hat{H}t/\hbar}\hat{B}e^{-i\hat{H}t/\hbar}\right]$.

1. Linearized semiclassical mapping dynamics

The LSC approximation of the time correlation function $C_{\hat{A}\hat{B}}(t)$ is given by[46,50,76–85]

$$C_{\hat{A}\hat{B}}(t) \approx \left(\frac{1}{2\pi\hbar}\right)^{N+F} \int d\mathbf{R}_0 d\mathbf{P}_0 d\mathbf{q}_0 d\mathbf{p}_0$$
$$\times [\rho_N(0)]_W(\mathbf{R}_0, \mathbf{P}_0)A_W(\mathbf{q}_0, \mathbf{p}_0)B_W(\mathbf{q}_t, \mathbf{p}_t). \quad (7)$$

LSC mapping is based on the Wigner transform of the quantum operator defined as

$$A_W(\mathbf{q}, \mathbf{p}) = \int d\mathbf{z}\, e^{-i\mathbf{z}\cdot\mathbf{p}/\hbar}\left\langle\mathbf{q} + \frac{\mathbf{z}}{2}\middle|\hat{A}(\hat{\mathbf{q}}, \hat{\mathbf{p}})\middle|\mathbf{q} - \frac{\mathbf{z}}{2}\right\rangle. \quad (8)$$

There exist two mapping strategies,[52] including mapping No. 1,

$$[M_{jj}]_W^{(1)}(\mathbf{q}, \mathbf{p}) = \frac{1}{2\hbar}\left(q_j^2 + p_j^2 - \hbar\right),$$
$$[M_{kj}]_W^{(1)}(\mathbf{q}, \mathbf{p}) = \frac{1}{2\hbar}(q_k - ip_k)(q_j + ip_j), \quad (9)$$

and mapping No. 2,

$$[M_{jj}]_W^{(2)}(\mathbf{q}, \mathbf{p}) = \frac{1}{2\hbar}\left(q_j^2 + p_j^2 - \frac{\hbar}{2}\right)G(\mathbf{q}, \mathbf{p}),$$
$$[M_{kj}]_W^{(2)}(\mathbf{q}, \mathbf{p}) = \frac{1}{2\hbar}(q_k - ip_k)(q_j + ip_j)G(\mathbf{q}, \mathbf{p}), \quad (10)$$

where a phase-space function of Gaussian form is defined as

$$G(\mathbf{q}, \mathbf{p}) = 2^{F+2}\exp\left[-\frac{1}{\hbar}\sum_l^F\left(q_l^2 + p_l^2\right)\right]. \quad (11)$$

Here, $G(\mathbf{q}, \mathbf{p})$ can be used for initial sampling of the mapping variables $(\mathbf{q}_0, \mathbf{p}_0)$ and choosing mapping No. 1 or mapping No. 2 [superscript $(1)/(2)$] leads to **LSC1** and **LSC2** approximations (equivalent to PBME[51] and LSC-IVR,[45] respectively) to the electronic RDM $\sigma_{jk}(t)$ in Eq. (6),[52]

$$\sigma_{jk}^{\text{LSC1/2}}(t) = \left(\frac{1}{2\pi\hbar}\right)^{N+F}\sum_{m,n}^F \sigma_{mn}(0)\int d\mathbf{R}_0 d\mathbf{P}_0 d\mathbf{q}_0 d\mathbf{p}_0$$
$$\times [\rho_N(0)]_W(\mathbf{R}_0, \mathbf{P}_0)[M_{mn}]_W^{(2)}(\mathbf{q}_0, \mathbf{p}_0)$$
$$\times [M_{kj}]_W^{(1)/(2)}(\mathbf{q}_t, \mathbf{p}_t). \quad (12)$$

The initial sampling of the nuclear DOF is over the Wigner function

$$\rho_{N,W}(\mathbf{R}, \mathbf{P}) = \int d\mathbf{Z}\, e^{-i\mathbf{Z}\cdot\mathbf{P}/\hbar}\left\langle\mathbf{R} + \frac{\mathbf{Z}}{2}\middle|\hat{\rho}_N(0)\middle|\mathbf{R} - \frac{\mathbf{Z}}{2}\right\rangle, \quad (13)$$

which is also used in the rest of mapping dynamics.

For a better population dynamics, one casts the population in terms of the identity operator, $\hat{1}$, and the traceless operator, $\hat{Q}_j = F\hat{M}_{jj} - \sum_k^F \hat{M}_{kk}$, using the resolution of identity (RI) $\sum_j^F |j\rangle\langle j| = \hat{1}$ such that the population of state j is given by $|j\rangle\langle j| = \frac{1}{F}(\hat{1} + \hat{Q}_j)$.[42,86] The population and coherence become

$$\sigma_{jj}(t) = \frac{1}{F^2}\left[F + C_{\hat{1}\hat{Q}_j}(t) + C_{\hat{Q}_m\hat{Q}_j}(t)\right],$$
$$\sigma_{jk}(t) = \frac{1}{F}\left[C_{\hat{1}\hat{M}_{kj}}(t) + C_{\hat{Q}_m\hat{M}_{kj}}(t)\right]. \quad (14)$$

Using the RI tricks as in Eq. (14), the traceless operator can be written in terms of mapping No. 1 or No. 2 as follows:

$$[Q_j]_W^{(1)/(2)}(\mathbf{q}, \mathbf{p}) = F[M_{jj}]_W^{(1)/(2)}(\mathbf{q}, \mathbf{p}) - \sum_k^F [M_{kk}]_W^{(1)/(2)}(\mathbf{q}, \mathbf{p}). \quad (15)$$

Using $G(\mathbf{q}, \mathbf{p})$ in observables $\hat{Q}_j(t)$ or $\hat{M}_{kj}(t)$ for the initial sampling of the mapping variables, the three ways for treating $\hat{Q}_m(0)$ and the identity operator $\hat{1}$ lead to the following methods: **RI-LSC1** treats the identity operator as 1 and uses mapping No. 1 for $\hat{Q}_m(0)$; **RI-LSC2** treats the identity operator as 1 and uses mapping No. 2 for $\hat{Q}_m(0)$; and **RI-LSC3** treats the identity operator as $G(\mathbf{q}, \mathbf{p})$ given in Eq. (11) and uses mapping No. 2 for $\hat{Q}_m(0)$.[14,71] RI-LSC1 ~3 are also known as mLSC/$\phi^1\phi^1$, mLSC/$\phi^1\phi^2$, and mLSC/$\phi^2\phi^2$, respectively.[52,87–90]

2. Symmetrical quasiclassical mapping dynamics

The SQC dynamics proposed by Cotton and Miller provides a windowing approach for formulating the initial sampling and the RDM.[37,38,53,70,91,92] The Cartesian mapping variables can be expressed equivalently in terms of action–angle (a–a) variables, $(\mathbf{n}, \mathbf{u})$, where $\mathbf{n} = (n_1, \ldots, n_F)$ and $\mathbf{u} = (u_1, \ldots, u_F)$ such that n_j and u_j are the action and angle variables of the jth harmonic oscillator: $n_j = \frac{1}{2\hbar}(q_j^2 + p_j^2) - \gamma$, $u_j = -\arctan(p_j/q_j)$. Taking the Wigner transform of electronic operators $|k\rangle\langle j|$ in terms of a–a variables, $[M_{kj}]_W(\mathbf{n}, \mathbf{u}) = \int d\mathbf{y} e^{-i\mathbf{y}\cdot\mathbf{n}}\langle \mathbf{u} + \mathbf{y}/2|\hat{M}_{kj}|\mathbf{u} - \mathbf{y}/2\rangle$, we have

$$[M_{jj}]_W(\mathbf{n}, \mathbf{u}) = \delta(n_j - 1)\prod_{l\neq j}^F \delta(n_l),$$

$$[M_{kj}]_W(\mathbf{n}, \mathbf{u}) = e^{i(u_j - u_k)}\delta\left(n_j - \frac{1}{2}\right)\delta\left(n_k - \frac{1}{2}\right)\prod_{l\neq j,k}^F \delta(n_l). \quad (16)$$

In the SQC method, the delta functions in Eq. (16) are replaced with finite-width window functions, and the two popular choices are square windows[37] or triangle windows.[38] The **SQC-square** uses window function $w_a(n_j) = h(\gamma - |n_j - a|)$, where $h(x)$ is the Heaviside step function and the reported optimal ZPE parameter value $\gamma = 0.366$ for the square window[37] is used,

$$[M_{jj}]_W^{(\text{SQC-sq})}(\mathbf{n}, \mathbf{u}) = w_1(n_j)\prod_{l\neq j}^F w_0(n_l),$$

$$[M_{kj}]_W^{(\text{SQC-sq})}(\mathbf{n}, \mathbf{u}) = e^{i(u_j - u_k)}w_{\frac{1}{2}}(n_k)w_{\frac{1}{2}}(n_j)\prod_{l\neq j,k}^F w_0(n_l). \quad (17)$$

The **SQC-triangle** uses the window function with the reported optimal value $\gamma = 1/3$,[38]

$$[M_{jj}]_W^{(\text{SQC-tri})}(\mathbf{n}, \mathbf{u}) = w_1(n_j)\prod_{l\neq j}^F w_0(n_j, n_l),$$

$$[M_{kj}]_W^{(\text{SQC-tri})}(\mathbf{n}, \mathbf{u}) = e^{i(u_j - u_k)}w_{\frac{1}{2}}(n_k)w_{\frac{1}{2}}(n_j)\prod_{l\neq j,k}^F w_0(n_{j,k}, n_l), \quad (18)$$

where $w_a(n_j) = (2 - \gamma - n_j)^{2-F}$ when $(-\gamma < n - a < 1 - \gamma)$ and vanishes otherwise; $w_0(n_j, n_l) = 1$ when $(n_l < 2 - 2\gamma - n_j)$ and vanishes otherwise. It is typically recommended to use the triangle window within SQC.[38]

The initial values of the action mapping variables $\mathbf{n}$ are sampled randomly within the initial window, while the angle mapping variables $\mathbf{u}$ are sampled uniformly in $[0, 2\pi]$. During propagation, the a–a variables can be transformed back to the Cartesian mapping variable $(\mathbf{q}, \mathbf{p})$ via relations $q_j = \sqrt{2(n_j + \gamma)\hbar}\cos(u_j)$ and

$p_j = -\sqrt{2(n_j + \gamma)\hbar}\sin(u_j)$ such that the equations of motion are the same as LSC mapping dynamics. To ensure that the total population is one for all time, the RDM elements should be renormalized via $\sigma_{jk}(t) = \sigma_{jk}^{\text{raw}}(t)/\sum_l^F \sigma_{ll}^{\text{raw}}(t)$, where $\sigma_{jk}^{\text{raw}}(t)$ is the raw electronic reduced density matrix element at time t. The diabatic representation is chosen over the adiabatic representation for the mapping dynamics calculations in this work.[91,93]

3. Extended classical mapping model and spin-mapping model

The eCMM method[39,59,60,75] can be formulated in terms of the mapping Hamiltonian in Eq. (4), but the initial conditions of the mapping variables are uniformly sampled over the full-sphere,

$$\mathcal{S}(\gamma): \quad \sum_{j=1}^F \frac{1}{2\hbar}(q_j^2 + p_j^2) = 1 + F\gamma. \quad (19)$$

If the initial electronic RDM is $\hat{\sigma}(0) = |m\rangle\langle m|$, then the population of the nth state at time t is given by

$$P_{m\to n}(t) = \text{Tr}_N \text{Tr}_e\left[\hat{\rho}_N(0)|m\rangle\langle m|e^{i\hat{H}t/\hbar}|n\rangle\langle n|e^{-i\hat{H}t/\hbar}\right]$$

$$= \frac{1}{(2\pi\hbar)^N}\int d\mathbf{R}_0 d\mathbf{P}_0 \rho_{N,W}(\mathbf{R}_0, \mathbf{P}_0)$$

$$\times \int_{\mathcal{S}(\gamma)} F d\mathbf{q}_0 d\mathbf{p}_0\left[\frac{1}{2\hbar}(q_m(0)^2 + p_m(0)^2) - \gamma\right]$$

$$\times \left[\frac{Q(\tilde{\gamma}, \gamma)}{2\hbar}(q_n(t)^2 + p_n(t)^2) - \tilde{\gamma}\right], \quad (20)$$

where $\tilde{\gamma} = \frac{1-\gamma}{1+F\gamma}$ and $Q(\tilde{\gamma}, \gamma) = \frac{1+F\tilde{\gamma}}{1+F\gamma} = \frac{1+F}{(1+F\gamma)^2}$.

The SPM method has Q, P, and W representations,[41] which are equivalent to eCMM with $\gamma = 0$, 1, $(\sqrt{F+1} - 1)/F$, respectively. It is straightforward to show when $\gamma = (\sqrt{F+1} - 1)/F$ as in the W-representation SPM, $\tilde{\gamma} = \gamma$ and $Q(\tilde{\gamma}, \gamma) = 1$ such that the initial and final electronic population expressions become identical. It is noted that the W scheme of SPM is recommended in the literature,[41] and we keep the P, Q, W labels to mark the correspondence of the special γ values in eCMM.

The Q, P, W schemes of SPM could also use focused initial sampling for the mapping variables, which are denoted as Q-foc, P-foc, and W-foc, respectively. In the case of $\hat{A} = |m\rangle\langle m|$, $\hat{B} = |k\rangle\langle j|$, the focused distribution is given by

$$\rho_{\text{foc}}(\mathbf{q}, \mathbf{p}) = \prod_{j=1}^F \delta\left(\frac{1}{2\hbar}(q_j^2 + p_j^2) - \gamma - \delta_{jm}\right). \quad (21)$$

Then, $A_W(\mathbf{q}, \mathbf{p}) = 1$, $B_W(\mathbf{q}, \mathbf{p}) = \frac{1}{2\hbar}(q_k - ip_k)(q_j + ip_j) - \gamma\delta_{kj}$, and the time correlation function is given by

$$C_{\hat{A}\hat{B}}(t) = \frac{1}{(2\pi\hbar)^N}\int d\mathbf{R}_0 d\mathbf{P}_0 \rho_{N,W}(\mathbf{R}_0, \mathbf{P}_0)$$

$$\times \frac{1}{Z_{\text{foc}}}\int d\mathbf{q}_0 d\mathbf{p}_0 \rho_{\text{foc}}(\mathbf{q}_0, \mathbf{p}_0)B_W(\mathbf{q}_t, \mathbf{p}_t), \quad (22)$$

where $Z_{\text{foc}} = \int d\mathbf{q}d\mathbf{p}\rho_{\text{foc}}(\mathbf{q}, \mathbf{p})$. The MMST-foc scheme in our implementation corresponds to the case when $\gamma = \tilde{\gamma} = 1/2$ and $Q(\tilde{\gamma}, \gamma) = 1$.[40,41]

4. Mean-field Ehrenfest dynamics

Ehrenfest dynamics treats the nuclear and electronic DOF in a mean-field manner.[94,95] The time-dependent wave function can be expanded as a linear combination of electronic states, i.e., $|\Psi(t)\rangle = \sum_j c_j(t)|\psi_j\rangle$ with expansion coefficients $\{c_j(t)|j = 1, \ldots, F\}$. The equation of motion for the electronic RDM, $\sigma_{jk}(t) = c_j(t)c_k^*(t)$, is given by the quantum Liouville equation $\frac{\partial}{\partial t}\hat{\sigma}(t) = -\frac{i}{\hbar}[\hat{V}(\mathbf{R}_t), \hat{\sigma}(t)]$. The electronic propagation can be expressed as $\hat{\sigma}(t + \Delta t) = e^{-i\delta t \hat{V}(\mathbf{R}_t)/\hbar}\hat{\sigma}(t)e^{i\delta t \hat{V}(\mathbf{R}_t)/\hbar}$ $= \hat{U}(t + \Delta t, t)\hat{\sigma}(t)\hat{U}^\dagger(t + \Delta t, t)$. Here, the time evolution operator $\hat{U}(t + \Delta t, t)$ in the diabatic basis can be expressed in terms of adiabatic energies and transformation matrix $\mathbf{T}$ that diagonalizes $\hat{V}(\mathbf{R}_t)$ such that $\mathbf{T}^\dagger \hat{V}(\mathbf{R}_t)\mathbf{T} = \text{diag}(E_1, \ldots, E_F)$: $\hat{U}(t + \Delta t, t) = \mathbf{T}\,\text{diag}(e^{-iE_1\Delta t/\hbar}, \ldots, e^{-iE_F\Delta t/\hbar})\mathbf{T}^\dagger$. Moreover, the nuclear equations of motion are given by $\dot{\mathbf{R}} = \mathbf{P}$, $\dot{\mathbf{P}} = -\frac{\partial}{\partial \mathbf{R}}V_{\text{mf}}(\mathbf{R}) = \mathbf{F}_{\text{mf}}(\mathbf{R})$, where the mean-field potential is $V_{\text{mf}}(\mathbf{R}_t) = \sum_{j,k}^F \sigma_{jk}(t)V_{kj}(\mathbf{R}_t)$.[71] Although the equations of motion can also be formed the same way as in the above-mentioned mapping dynamics with $\gamma = 0$, Ehrenfest dynamics has no initial sampling for the electronic DOF since the initial electronic RDM elements $\sigma_{jk}(0)$ are known.

5. Fewest switches surface hopping dynamics

Within the FSSH method, the electronic expansion coefficient dynamics are dictated by the equation of motion derived from the time-dependent Schrödinger equation:[96]

$$\frac{dc_a}{dt} = -\sum_b c_b\left(\frac{i}{\hbar}V_{ab}(\mathbf{R}) + \mathbf{d}_{ab}\cdot\dot{\mathbf{R}}\right), \tag{23}$$

where the nonadiabatic coupling (NAC) vector is defined as $\mathbf{d}_{ab} = \langle\psi_a|\nabla_\mathbf{R}\psi_b\rangle$, $\dot{\mathbf{R}}$ is the nuclear velocity, and $\langle\psi_a|\frac{\partial}{\partial t}|\psi_b\rangle = \mathbf{d}_{ab}\cdot\dot{\mathbf{R}}$. In surface hopping dynamics, only one electronic state can be the active state at a time and the nuclear dynamics are determined by the active state, $|\psi_a\rangle$, where the effective forces on the nuclear DOF from the active state's PES are given by

$$\mathbf{F}_a^{\text{FSSH}}(t) = -\left\langle\psi_a\left|\frac{\partial}{\partial \mathbf{R}}\hat{V}(\mathbf{R})\right|\psi_a\right\rangle = \dot{\mathbf{P}}(t). \tag{24}$$

The active state can be determined by the hopping process from the current active state, $|\psi_a\rangle$, to another state, $|\psi_b\rangle$, with the transition probability,

$$P_{a\to b} = \max[0, g_{a\to b}(t)], \tag{25}$$

$$g_{a\to b} = \frac{2\Delta t}{\sigma_{aa}}[\text{Im}(V_{ab}\sigma_{ba})/\hbar - \text{Re}(\mathbf{d}_{ab}\cdot\dot{\mathbf{R}}\sigma_{ba})], \tag{26}$$

where Δt serves as nuclear integration step length and electronic density matrix elements $\sigma_{ba} = c_b c_a^*$. To determine whether a hopping from state $|\psi_a\rangle$ to $|\psi_b\rangle$ occurs, a uniformly distribution random number $\zeta \sim U(0, 1)$ is sampled and the transition is accepted if ζ satisfies

$$\sum_{j=1}^{b-1} P_{a\to j} \leq \zeta < \sum_{j=1}^{b} P_{a\to j}. \tag{27}$$

When the adiabatic basis is used such as in Tully's models, the off-diagonal potential energy elements V_{ab} vanish and thus the first term in $g_{a\to b}$ vanishes, whereas in the diabatic basis that was employed in the other models here, the NAC vanishes, and thus, the second term in $g_{a\to b}$ vanishes [Eq. (26)]. After a hopping, the nuclear momenta should be adjusted such that the total energy is conserved, which means that the kinetic energy should be added $\Delta E_{ab} = \langle\psi_a|V(\mathbf{R})|\psi_a\rangle - \langle\psi_b|V(\mathbf{R})|\psi_b\rangle$, so the momenta are scaled as $\mathbf{P}' \to \eta\mathbf{P}$, where $\eta = \sqrt{2\Delta E_{ab}/\mathbf{P}^2 + 1}$. However, if a hop is to an energetically higher state but the system has no sufficient kinetic energy, the transition will be aborted, also known as the frustrated hop.

B. Numerically exact wavepacket dynamics with tensor-train approaches

The numerically exact methods that will be employed in this study are the tensor-train (TT) based wavepacket dynamics approaches. In this subsection, we first briefly explain the TT format that facilitates the storage of and operations on high-dimensional wavepacket and then introduce the TT-SOKSL and TT-TFD methods used for zero temperature and finite temperature real-time wavepacket propagations, respectively.

1. Tensor-train wavepacket

Consider a general time-dependent wavepacket with d degrees of freedom, $|\Psi(t)\rangle$, which can be expanded as follows:

$$|\Psi(t)\rangle = \sum_{j_1,\ldots,j_d}^{n_1,\ldots,n_d} X(t; j_1, \ldots, j_d)|j_1\rangle\ldots|j_d\rangle, \tag{28}$$

where $\{|j_k\rangle\}$ with $k = 1, \ldots, d$ is the basis set of size n_k for the kth physical degree of freedom and $X(t)$ is a d-dimensional array that stores all $n_1 \times \cdots \times n_d$ time-dependent expansion coefficients. The size of X (time variable omitted henceforth) grows exponentially with d, causing the operation and storage of $|\Psi(t)\rangle$ with $d > 10$ intractable in the standard grid-based representation. The tensor-train methodology provides a numerically accurate way of representing the high-dimensional X with a train of three-dimensional arrays whose size scales linearly with d and therefore bypasses the so-called curse of dimensionality. The TT format of the complex $n_1 \times \cdots \times n_d$ array X involves d three-dimensional complex arrays X_k of size $r_{k-1} \times n_k \times r_k$ for $k = 1, \ldots, d$, with $r_0 = r_d = 1$, such that any element of X, namely, $X(j_1, \ldots, j_d)$, is approximated by the following tensor product:

$$X(j_1, \ldots, j_d) = \sum_{a_0,\ldots,a_d}^{r_0,\ldots,r_d} X_1(a_0, j_1, a_1)X_2(a_1, j_2, a_2)$$
$$\cdots X_d(a_{d-1}, j_d, a_d), \tag{29}$$

which is equivalently expressed in the matrix product state form,

$$X(j_1, \ldots, j_d) = \mathbf{X}_1(j_1)\mathbf{X}_2(j_2)\cdots\mathbf{X}_d(j_d), \tag{30}$$

where the $r_{k-1} \times r_k$ matrix $\mathbf{X}_k(j_k)$ is the j_kth slice of the $r_{k-1} \times n_k \times r_k$ core tensor X_k. According to Eq. (29), every element of X is obtained only with the three-dimensional tensors $X_1, \ldots, X_d$. If $r_1 = \cdots = r_{d-1} = \tilde{r}$ and $n_1 = \cdots = n_d = n$, then only $dn\tilde{r}^2$ elements are required to be stored explicitly. The set $\{r_k\}$ thus determines the storage with given n and d and is hence referred as TT-rank in analogy with the matrix rank.

2. Tensor-train split-operator KSL (TT-SOKSL) method for zero-temperature real-time propagation

The TT-SOKSL method integrates the time-dependent Schrödinger equation,

$$\frac{d}{dt}|\Psi(t)\rangle = -\frac{i}{\hbar}\hat{H}|\Psi(t)\rangle, \tag{31}$$

where $\hat{H} = \hat{T} + \hat{V}$ is the total Hamiltonian and $|\Psi(t)\rangle$ is the TT wavepacket as introduced in Eqs. (28)–(30) with $\{|j_k\rangle\}$ in Eq. (28) being the standard position grid basis. Similar to the SOFT method, TT-SOKSL integrates Eq. (31) to the second-order accuracy with the Strang splitting method, which approximately evolves the wavepacket from $|\Psi(t_k)\rangle$ to $|\Psi(t_{k+1})\rangle$ for time step $\Delta t = t_{k+1} - t_k$ by solving the following sequence of differential equations:

(1) Integrate equation:

$$\frac{d}{dt}|\Psi_1(t)\rangle = -\frac{i\hat{V}}{2\hbar}|\Psi_1(t)\rangle, \tag{32}$$

from $t = t_k$ to $t = t_{k+1}$, with initial condition $|\Psi_1(t_k)\rangle = |\Psi(t_k)\rangle$ to obtain $|\Psi_1(t_{k+1})\rangle$.

(2) Integrate equation:

$$\frac{d}{dt}|\Psi_2(t)\rangle = -\frac{i\hat{T}}{\hbar}|\Psi_2(t)\rangle, \tag{33}$$

from $t = t_k$ to $t = t_{k+1}$, with initial condition $|\Psi_2(t_k)\rangle = |\Psi_1(t_{k+1})\rangle$ to obtain $|\Psi_2(t_{k+1})\rangle$.

(3) Integrate equation:

$$\frac{d}{dt}|\Psi_3(t)\rangle = -\frac{i\hat{V}}{2\hbar}|\Psi_3(t)\rangle, \tag{34}$$

from $t = t_k$ to $t = t_{k+1}$, with initial condition $|\Psi_3(t_k)\rangle = |\Psi_2(t_{k+1})\rangle$ to obtain $|\Psi_3(t_{k+1})\rangle$, which gives the approximate solution $|\Psi(t_{k+1})\rangle = |\Psi_3(t_{k+1})\rangle + O(\Delta t^3)$.

TT-SOKSL integrates Eqs. (32)–(34) sequentially with the TT-KSL integrator in combination with the SOFT approach. In Eq. (32), the wavepacket $|\Psi_1(t)\rangle$ is in the position space representation, under which the position operator $-i\hat{V}/2\hbar$ is a diagonal operator. Therefore, the integration of Eq. (32) is carried out with the TT-KSL integrator with an efficient TT diagonal matrix–vector multiplication or equivalently an elementwise TT vector–vector multiplication instead of the usual TT matrix–vector multiplication. The resulting $|\Psi_1(t_{k+1})\rangle$ is then Fourier transformed to the momentum space so that the integration of Eq. (33) with kinetic operator $-i\hat{T}/\hbar$ is also carried out with an TT vector–vector multiplication. The resulting $|\Psi_2(t_{k+1})\rangle$ is then inverse Fourier transformed back to the position space, and the integration of Eq. (34) is carried out in a manner similar to that of Eq. (32). To sum up, a complete TT-SOKSL integration step is performed with the following equation:

$$|\Psi(\mathbf{x}, t_{k+1})\rangle = \text{KSL}\big(\Delta t, -i\hat{V}(\mathbf{x})/2\hbar, \text{IFT}\big[\text{KSL}\big(\Delta t, -i\hat{T}(\mathbf{p})/\hbar$$
$$\text{FT}\big[\text{KSL}\big(\Delta t, -i\hat{V}(\mathbf{x}')/2\hbar, |\Psi(\mathbf{x}', t_k)\rangle\big)\big]\big)\big]\big), \tag{35}$$

where KSL denotes one substep of rank-adaptive TT-KSL propagation.

3. Tensor-train thermofield dynamics (TT-TFD) method for finite-temperature real-time propagation

The TT-TFD method solves the quantum Liouville equation,

$$\frac{d}{dt}\hat{\rho}(t) = -\frac{i}{\hbar}[\hat{H}, \hat{\rho}(t)], \tag{36}$$

by transforming the density operator $\hat{\rho}(t)$ from a matrix in the physical Hilbert space to a vector in the so-called "double space" and consecutively transforming Eq. (36) to a commutator-free differential equation that takes a form similar to Eq. (31), whose integration provides all dynamical information of the system at finite temperature. In this study, the density matrix is initiated at the initial thermal equilibrium distribution, and the Schrödinger-like propagation of its corresponding finite-temperature double space state vector is therefore seen as a finite-temperature wavepacket propagation.

To help writing the density matrix $\hat{\rho}(t)$ as a state vector, we define the double space unit vector $|I\rangle$,

$$|I\rangle = \sum_{i=\tilde{i}}|i\rangle \otimes |\tilde{i}\rangle, \tag{37}$$

where $i = \tilde{i}$ indexes over the basis vectors of the system's Hilbert space $\mathcal{H}$ and $|\tilde{i}\rangle$ is an exact copy of $|i\rangle$, expanding a "fictional space" that is an exact copy of $\mathcal{H}$. Therefore, $|I\rangle$ defined in the double space has dimensionality twice that of $\mathcal{H}$. With $|I\rangle$, we define the initial thermal wavepacket $|0(\beta)\rangle$,

$$|0(\beta)\rangle = \frac{e^{-\beta\hat{H}_n/2}}{\sqrt{Z(\beta)}}|I\rangle, \tag{38}$$

from which the thermal equilibrium density matrix $\hat{\rho}(0, \beta) = e^{-\beta\hat{H}}/\text{Tr}\{e^{-\beta\hat{H}}\} \equiv e^{-\beta\hat{H}}/Z(\beta)$ is fully recovered upon taking outer product with its dual and tracing out the fictional DOF,

$$\hat{\rho}(0, \beta) = \text{Tr}_f\{|0(\beta)\rangle\langle 0(\beta)|\}. \tag{39}$$

Furthermore, we define the finite-temperature double-space wavepacket $|\psi(\beta, t)\rangle$ according to the initial value $|\psi(\beta, 0)\rangle = |0(\beta)\rangle$, and the equation of motion is given by

$$\frac{d|\psi(\beta, t)\rangle}{dt} = -\frac{i}{\hbar}\bar{H}|\psi(\beta, t)\rangle, \tag{40}$$

where $\bar{H} = \hat{H} \otimes \tilde{1}$, with $\tilde{1}$ being the fictional space identity operator. With this definition, it is readily verified that the time-evolved density matrix $\hat{\rho}(t)$ is recovered from $|\psi(\beta, t)\rangle$,

$$\hat{\rho}(t) = \text{Tr}_f\{|\psi(\beta, t)\rangle\langle\psi(\beta, t)|\}. \tag{41}$$

Therefore, $\hat{\rho}(t)$ as well as all corresponding dynamical observables are obtained by propagating $|\psi(\beta, t)\rangle$ according to Eq. (40). Furthermore, all physical dynamical observables are invariant upon redefining $\bar{H}$ in Eq. (40) as $\bar{H} = \hat{H} \otimes \tilde{1} - \hat{1} \otimes \tilde{H}_f$, where $\tilde{H}_f$ is an arbitrary operator in the fictional space. This replacement provides mathematical flexibility necessary for a more compact equation of motion for model systems investigated in this study.

The preparation of the initial state $|\psi(\beta, 0)\rangle$ as in Eq. (38) requires imaginary time propagation, which could be computationally burdensome. However, when the Hamiltonian is harmonic, we can choose

$$\bar{H} = \hat{H} \otimes \tilde{I} - \hat{I} \otimes \sum_j \omega_j \tilde{a}_j^\dagger \tilde{a}_j. \tag{42}$$

This task is circumvented utilizing the thermal Bogoliubov transformation, which provides the matrix $\hat{G}$ that rotates the double-space vacuum state $|0, \tilde{0}\rangle = |0\rangle \otimes |\tilde{0}\rangle$ to $|0(\beta)\rangle$,

$$|0(\beta)\rangle = e^{-i\hat{G}} |0, \tilde{0}\rangle, \tag{43}$$

where

$$\hat{G} = -i \sum_j \theta_j \left(\hat{a}_j \tilde{a}_j - \hat{a}_j^\dagger \tilde{a}_j^\dagger \right), \tag{44}$$

$\theta_j = \mathrm{arctanh}(e^{-\beta\omega_j/2})$, and $\hat{a}_j, \hat{a}_j^\dagger$ $(\tilde{a}_j, \tilde{a}_j^\dagger)$ are the physical (fictional) bosonic creation and annihilation operators for the jth degree of freedom. Substituting Eqs. (43) and (44) into Eq. (40), we obtain

$$\frac{d|\psi_\theta(\beta, t)\rangle}{dt} = -\frac{i}{\hbar} \bar{H}_\theta |\psi_\theta(\beta, t)\rangle, \tag{45}$$

where

$$\begin{aligned} \bar{H}_\theta &= e^{i\hat{G}} \bar{H} e^{-i\hat{G}}, \\ |\psi_\theta(\beta, 0)\rangle &= e^{i\hat{G}} |\psi(\beta, 0)\rangle = |0, \tilde{0}\rangle. \end{aligned} \tag{46}$$

TT-TFD expresses $|0, \tilde{0}\rangle$ as a rank-1 tensor train [Eq. (30)] and propagates Eq. (45) to obtain $|\psi_\theta(\beta, t)\rangle$. The propagation is carried out with the TT-KSL integrator. The expectation value of any physical observable $\hat{A} \in \mathcal{H}$ is given by

$$\langle A(t) \rangle = \langle \psi_\theta(\beta, t) | \bar{A}_\theta | \psi_\theta(\beta, t) \rangle, \tag{47}$$

where $\bar{A}_\theta = e^{i\hat{G}} \bar{A} e^{-i\hat{G}}$ and $\bar{A} = \hat{A} \otimes \tilde{I}$.

III. MODELS

A. Spin-boson models

The spin-boson model Hamiltonian for a two-level system with the donor state $|D\rangle$ and the acceptor state $|A\rangle$ can be expressed as follows:

$$\hat{H} = \Gamma \hat{\sigma}_x + \varepsilon \hat{\sigma}_z + \sum_{j=1}^N \left(\frac{\hat{P}_j^2}{2} + \frac{1}{2} \omega_j^2 \hat{R}_j^2 - c_j \hat{R}_j \hat{\sigma}_z \right). \tag{48}$$

Here, $\hat{\sigma}_x = |D\rangle\langle A| + |A\rangle\langle D|$ and $\hat{\sigma}_z = |D\rangle\langle D| - |A\rangle\langle A|$ are the Pauli matrices; Γ is the electronic coupling that is assumed to be constant in the Condon approximation; $\Delta E = -2\varepsilon$ is the donor-to-acceptor reaction free energy; $\{\hat{R}_j, \hat{P}_j, \omega_j\} = \{\hat{R}_j, \hat{P}_j, \omega_j | j = 1, \ldots, N\}$ are the mass-weighted coordinates, momenta, and frequencies associated with the N nuclear normal modes, respectively; and $\{c_j\}$ are the electronic-vibrational coupling coefficients. The mode frequencies and the electronic-vibrational coupling coefficients $\{\omega_j, c_j\}$ are determined by discretizing the spectral density defined as

$$J(\omega) = \frac{\pi}{2} \sum_{j=1}^N \frac{c_j^2}{\omega_j} \delta(\omega - \omega_j). \tag{49}$$

The spectral density can be assumed to be in a closed-form expression with empirical parameters[6,97–100] or obtained from taking Fourier transform of the time correlation function of the energy gap fluctuations in all-atom molecular dynamics (MD).[9,101] In this work, we employ the Ohmic spectral density, which is given by

$$J(\omega) = \frac{\pi}{2} \hbar \xi \omega e^{-\omega/\omega_c}, \tag{50}$$

where ξ is the Kondo parameter and ω_c is the cutoff frequency. The displacement between the donor and acceptor equilibrium geometry along the jth mode is $R_j^{eq} = 2c_j/\omega_j^2$ $(j = 1, \ldots, N)$. The reorganization energy between the two states is given by

$$\begin{aligned} E_r &= \frac{4}{\pi} \int_0^\infty d\omega \frac{J(\omega)}{\omega} \\ &= \frac{1}{2} \sum_{j=1}^N \omega_j^2 (R_j^{eq})^2 = 2 \sum_{j=1}^N \frac{c_j^2}{\omega_j^2}. \end{aligned} \tag{51}$$

In this work, we will examine nine spin-boson models, ranging from biased and unbiased energetic driving forces, small and large reorganization energies, as well as different electronic coupling strengths as summarized in Table I. Here, models No. 1–No. 4 and No. 9 are defined with the same electronic coupling $\Gamma = 1$, while ϵ and ξ are varied. Models No. 5–No. 8 are all biased cases with a downhill reaction free energy but different Γ and ξ parameters. It is noted that a larger ξ leads to a larger reorganization energy since $E_r \sim 2\hbar\xi\omega_c$. We categorize the spin-boson models in terms of adiabatic vs nonadiabatic regimes according to the ratio ω_c/Γ: the adiabatic regime ($\omega_c/\Gamma < 1$) features large electronic coupling and slow nuclear motion, whereas the nonadiabatic regime ($\omega_c/\Gamma > 1$) features small electronic coupling and fast nuclear motion.[102] As shown in Table S1, spin-boson model No. 1 is in the intermediate regime ($\omega_c/\Gamma = 1$), models No. 2–6 are in the nonadiabatic regime, and models No. 7–9 are in the adiabatic regime. In the Marcus weak-coupling nonadiabatic limit, we further categorize the models into the normal region ($-\Delta E < E_r$) and inverted region ($-\Delta E > E_r$). Thus, models No. 2, No. 3, and No. 5 are in the inverted region, while models No. 4 and No. 6 are in the normal region. The nuclear tunneling effects are expected to be more significant in the inverted region than the normal region at the nonadiabatic limit and also expected when the barrier is thin at the adiabatic limit.

The initial electronic state is set to be in the donor state, whereas the initial nuclear state is in equilibrium with the donor-state PES for models No. 1–No. 4 and No. 9, in equilibrium with the unshifted bath Hamiltonian for models No. 5–No. 8,

$$\hat{H}_b = \sum_{j=1}^N \frac{P_j^2}{2} + \frac{1}{2} \omega_j^2 R_j^2. \tag{52}$$

TABLE I. Spin-boson models' parameters, including energy offset ϵ, electronic coupling Γ, Kondo parameter ξ, and cutoff frequency ω_c of Ohmic spectral density, maximum frequency ω_{max}, the number of nuclear modes N, and time step dt in propagation. Here, models No. 1 to No. 4 adopted from Ref. 103 and model No. 9 are given in the reduced unit, and models No. 5 to No. 8 adopted from Ref. 104 are given with energy unit in cm^{-1}.

Model No.	ϵ	Γ	E_r	ξ	ω_c	ω_{max}	N
1	1.0	1.0	0.198	0.1	1.0	5.0	60
2	1.0	1.0	0.397	0.1	2.0	10.0	60
3	1.0	1.0	1.488	0.1	7.5	36.0	60
4	0	1.0	0.992	0.2	2.5	12.0	60
9	1.0	1.0	0.080	0.08	0.5	5.0	60
5	50	20	39.73	$20/\omega_c$	53	265	60
6	50	20	119.2	$60/\omega_c$	53	265	60
7	50	100	79.46	$40/\omega_c$	53	265	60
8	50	100	198.6	$100/\omega_c$	53	265	60

In the nonadiabatic mapping methods, the initial nuclear positions and momenta, $\{\mathbf{R}_0, \mathbf{P}_0\}$, were sampled from the semiclassical Wigner function at finite temperature,

$$\rho_W^{(i)}(\mathbf{R}_0, \mathbf{P}_0) = \prod_j^N \frac{1}{\pi\hbar} \tanh\left(\frac{\beta\hbar\omega_j}{2}\right) \exp\left[-\frac{2}{\hbar\omega_j}\right.$$
$$\left. \times \tanh\left(\frac{\beta\hbar\omega_j}{2}\right) H_i(\mathbf{R}_0, \mathbf{P}_0)\right], \quad (53)$$

where $\beta = 1/k_B T$ and $H_i(\mathbf{R}_0, \mathbf{P}_0)$ is the classical nuclear Hamiltonian of $|i\rangle$, on which PES the nuclear initial conditions are sampled. The initial nuclear sampling at zero temperature corresponds to the limit as $\beta \to \infty$,

$$\rho_W^{(i)}(\mathbf{R}_0, \mathbf{P}_0) = \prod_j^N \frac{1}{\pi\hbar} \exp\left[-\frac{2}{\hbar\omega_j} H_i(\mathbf{R}_0, \mathbf{P}_0)\right]. \quad (54)$$

B. Linear vibronic coupling models

We consider the linear vibronic coupling (LVC) models for describing electronic transitions through conical intersections in the fulvene molecule, the 2,6-bis(methylene) adamantyl (BMA) radical cation, and the 2-methylene-6isopropylidene adamantyl (MIA) radical cation, whose parameters were adopted from Ref. 105. The LVC Hamiltonian is given by

$$\hat{H} = \hat{H}_D |D\rangle\langle D| + \hat{H}_A |A\rangle\langle A| + \hat{\Gamma}(|D\rangle\langle A| + |A\rangle\langle D|), \quad (55)$$

where the nuclear operators are

$$\hat{H}_D = \sum_{j=1}^N \frac{\hat{P}_j^2}{2} + \sum_{j=1}^N \frac{1}{2}\omega_j^2 \hat{R}_j^2 + \epsilon_D, \quad (56)$$

$$\hat{H}_A = \sum_{j=1}^N \frac{\hat{P}_j^2}{2} + \sum_{k=1}^N \left(\frac{1}{2}\omega_j^2 \hat{R}_j^2 + g_j \hat{R}_j\right) + \epsilon_A, \quad (57)$$

$$\hat{\Gamma} = \sum_{j=1}^N \gamma_j \hat{R}_j. \quad (58)$$

TABLE II. Linear vibronic coupling (LVC) model parameters, including the number of nuclear modes N, reorganization energy E_r, reaction free energy ΔE, initial electronic state, and initial nuclear state (energy unit in a.u.).

	Fulvene	BMA	MIA
N	30	78	96
E_r	0.0887	0.0297	0.0274
ΔE	0.0989	−0.0004	−0.0250
Init. elec. state	$|A\rangle$	$|D\rangle$	$|D\rangle$
Init. nucl. state	V_D	V_A	V_A

Here, $\{\hat{R}_j, \hat{P}_j | j = 1, \ldots, N\}$ are the mass-weighted coordinates and momenta, N is the number of nuclear DOFs, the two electronic states are $|D\rangle$ and $|A\rangle$, $\{\omega_j\}$ are the nuclear mode frequencies, $\{g_j\}$ are the electronic-vibrational couplings, and $\epsilon_{D/A}$ are the minimum energies of PESs of the two electronic states. The important feature of the LVC model is the non-Condon diabatic coupling that depends on the current coordinates, and the linear diabatic coupling coefficients are $\{\gamma_j\}$. The equilibrium position of the jth nuclear mode on the acceptor state $|A\rangle$ is $R_j^{eq} = g_j/\omega_j^2$ $(j = 1, \ldots, N)$, and the reorganization energy is

$$E_r = \frac{1}{2}\sum_{j=1}^N \omega_j^2 (R_j^{eq})^2 = \frac{1}{2}\sum_{j=1}^N \frac{g_j^2}{\omega_j^2}. \quad (59)$$

The LVC model parameters of the three molecular systems and the initial electronic and nuclear states are summarized in Table II and the supplementary material with the mode-specific values of $\{\omega_j, g_j, \gamma_j\}$.

C. Retinal model

We consider a two-state 25-mode model Hamiltonian for the photoisomerization of the retinal chromophore in rhodopsin, which is a key process in vision. This retinal model adopted from Ref. 106 contains two primary modes, including the cis–trans reaction coordinate $\hat{R}_1 = \hat{\theta}$ that describes the anharmonic C$_{11}$═C$_{12}$

torsion and the linear coupling mode $\hat{R}_2 = \hat{R}_c$ that describes the polyene chain stretching, as well as 23 secondary harmonic bath modes $\{\hat{R}_j | j = 3, \ldots, 25\}$. The two electronic states $|0\rangle, |1\rangle$ correspond to S_0 and S_1 diabatic states that are linearly coupled. The retinal model Hamiltonian is given by

$$\hat{H} = \hat{H}_0 |0\rangle\langle 0| + \hat{H}_1 |1\rangle\langle 1| + \hat{V}_{01} |0\rangle\langle 1| + \hat{V}_{10} |1\rangle\langle 0|, \quad (60)$$

$$\hat{H}_0 = \frac{\hat{P}_\theta^2}{2I} + \frac{W_0}{2}(1 - \cos\hat{\theta}) + \frac{\Omega_c}{2}(\hat{P}_c^2 + \hat{R}_c^2) + \sum_{j=3}^{25} \frac{\omega_j}{2}(\hat{P}_j^2 + \hat{R}_j^2), \quad (61)$$

$$\hat{H}_1 = \frac{\hat{P}_\theta^2}{2I} + E_1 - \frac{W_1}{2}(1 - \cos\hat{\theta}) + \frac{\Omega_c}{2}(\hat{P}_c^2 + \hat{R}_c^2) + \kappa\hat{R}_c$$
$$+ \sum_{j=3}^{25} \frac{\omega_j}{2}(\hat{P}_j^2 + \hat{R}_j^2) + c_j\hat{R}_j, \quad (62)$$

$$\hat{V}_{01} = \hat{V}_{10} = \lambda\hat{R}_c. \quad (63)$$

Here, I is the moment of inertia, W_0 and W_1 are PES slopes of the rotational degree of freedom for $|0\rangle$ and $|1\rangle$, respectively, E_1 serves as the vertical shift of $|1\rangle$, Ω_c is the frequency of the coupling mode, $\hat{R}_c$, $\{\omega_j | j = 3, \ldots, 25\}$ is the frequencies of the bath modes, κ is the coupling coefficient between $\hat{R}_c$ and the electronic DOF, c_j are the coupling coefficients between the bath modes and the electronic DOF, and κ is the linear coupling coefficient in the off-diagonal diabatic coupling. The momenta of the primary modes are $\hat{P}_1 = \hat{P}_\theta = -i\frac{\partial}{\partial\theta}$ and $\hat{P}_2 = \hat{P}_c = -i\frac{\partial}{\partial R_c}$ ($\hbar = 1$).

The model parameters $\Omega_c = 1532$ cm^{-1} and the following parameters are in eV: $1/I = 4.84 \times 10^{-4}$, $E_1 = 2.48$, $W_0 = 3.6$, $W_1 = 1.09$, $\kappa = 0.1$, and $\lambda = 0.19$. The positions and momenta operators will be dimensionless in this case. The bath mode frequencies and electronic-vibrational couplings $\{\omega_j, c_j | j = 3, \ldots, 25\}$ (in cm^{-1}) are detailed in the supplementary material. For the photoisomerization reaction, the initial electronic state is the S_1 state and the initial nuclear condition is in equilibrium with the PES of the S_0 state. The initial state of the anharmonic primary mode θ corresponds to the normal distribution of $\rho(\theta) \propto e^{-\theta^2/(2\sigma_\theta^2)}$ where $\sigma_\theta = 0.152\,282\,75/2$.

D. Tully's models

Tully's models refer to a set of two-state one-dimensional models described by the total Hamiltonian $\hat{H} = \hat{T} + \hat{V}$ and electronic Hamiltonian $\hat{V} = \hat{V}_{00}|0\rangle\langle 0| + \hat{V}_{11}|1\rangle\langle 1| + \hat{V}_{01}|0\rangle\langle 1| + \hat{V}_{10}|1\rangle\langle 0|$, which is originally for testing scattering dynamics using the FSSH method.[107] It can be employed to benchmark various models for their ability to describe nuclear quantum effects.[52]

1. Single avoid crossing (SAC) model

The potential and coupling of the SAC model are given by

$$\hat{V}_{00}(x) = \begin{cases} A(1 - e^{-Bx}) & (x > 0), \\ -A(1 - e^{-Bx}) & (x < 0), \end{cases} \quad (64)$$

$$\hat{V}_{11}(x) = -\hat{V}_{00}(x), \quad (65)$$

$$\hat{V}_{01}(x) = \hat{V}_{10}(x) = Ce^{-Dx^2}, \quad (66)$$

where V_0 and V_1 represent PESs of $|0\rangle$ and $|1\rangle$, respectively, and V_{01} and V_{10} represent the diabatic couplings. Parameters $A = 0.01$, $B = 1.6$, $C = 0.005$, and $D = 1.0$. The initial state is on electronic state $|0\rangle$, and the nuclear initial position at $x_0 = -9$ and initial momentum $p_0 = 5, 10, 20$ is described by the Gaussian wavepacket,

$$\psi_0(x) = \left(\frac{1}{2\pi\sigma_x^2}\right)^{\frac{1}{4}} \exp\left[-\frac{(x - x_0)^2}{4\sigma_x^2} + \frac{i}{\hbar}p_0(x - x_0)\right], \quad (67)$$

which corresponds to the Wigner function for semiclassical initial sampling given by

$$\rho_W(x, p) = \frac{1}{2\pi\sigma_x\sigma_p} \exp\left[-\frac{(x - x_0)^2}{2\sigma_x^2} - \frac{(p - p_0)^2}{2\sigma_p^2}\right] \quad (68)$$

with $\sigma_x = 1/\sqrt{2}$ and $\sigma_p = \hbar/(2\sigma_x)$.

2. Dual avoid crossing (DAC) model

The potential and coupling of the SAC model are given by

$$\hat{V}_{00}(x) = 0, \quad (69)$$

$$\hat{V}_{11}(x) = -Ae^{-Bx^2} + E_0, \quad (70)$$

$$\hat{V}_{01}(x) = \hat{V}_{10}(x) = Ce^{-Dx^2}, \quad (71)$$

where parameters $A = 0.10$, $B = 0.28$, $C = 0.015$, $D = 0.06$, and $E_0 = 0.05$. The initial state is the same as in the SAC model, except the initial momentum $p_0 = 5, 15, 30$.

E. LCP model

The line cross parabola (LCP) model is a one-dimension two-state Hamiltonian[108] $\hat{H} = \hat{P}^2/2 + V(\hat{R})$, where $\hat{R}$ and $\hat{P}$ are the nuclear position and momentum, respectively, and the potential energy $V(\hat{R})$ is given by

$$V(\hat{R}) = \begin{bmatrix} V_1(\hat{R}) & \Gamma \\ \Gamma & V_2(\hat{R}) \end{bmatrix}. \quad (72)$$

Here, the electronic coupling is $\Gamma = 0.5$ and the parabola ($\omega = 1$) and the linear potentials are

$$V_1(\hat{R}) = \frac{1}{2}\omega^2 \hat{R}^2, \quad (73)$$

$$V_2(\hat{R}) = 6\hat{R} + 47.86. \quad (74)$$

The initial electronic state is the population on the parabola, i.e., $|1\rangle\langle 1|$. The initial nuclear state is chosen to be a certain vibrational eigenstate of the parabola, such as $n = 15$ and $n = 30$. In semiclassical simulations, the initial nuclear phase-space points are sampled from the microcanonical distribution with the fixed energy of the corresponding eigenstate, as $E_n = \hbar\omega(n + \frac{1}{2})$ for the nth eigenstate. With a random number ξ drawn from the uniform distribution in $[0, 2\pi]$, the initial positions and momenta are sampled according to

$$R = \sqrt{2E_n}\cos\xi, \quad (75)$$

11 July 2024 19:27:18

$$P = \sqrt{2E_n} \sin \xi. \qquad (76)$$

In the numerically exact simulation using SOFT, the initial wave function corresponding to the nth eigenstate is

$$\Psi_n(R) = \left(\frac{\alpha}{\pi}\right)^{\frac{1}{4}} H_n(\sqrt{\alpha}R) \exp\left(-\alpha R^2/2\right), \qquad (77)$$

where $\alpha = \omega/\hbar$ and $H_n(R)$ is the nth-order Hermite polynomial.

IV. SIMULATION DETAILS

A. Nonadiabatic mapping dynamics simulations

The simulations of nonadiabatic dynamics using mixed quantum–classical, semiclassical, and quasiclassical approximate methods employed here include mean-field Ehrenfest, FSSH, five versions of LSC mapping dynamics (LSC1–2, RI-LSC1–3), SQC (with square and triangle window), eCMM, and SPM (P, Q, W, MMST schemes). Among these methods, LSC methods use Gaussian sampling of mapping variables [Eq. (11)] and eCMM/SPM use full-sphere sampling of mapping variables [Eq. (19)], while focused sampling of mapping variables can be implemented with SQC windowing [Eqs. (17) and (18)] and SPM approaches [Eq. (21)], and no sampling of mapping variables is needed in MQC methods of Ehrenfest and FSSH dynamics. It is noted that the Ehrenfest method can be viewed as a nonadiabatic mapping dynamics with ZPE parameter $\gamma = 0$ since they share the equations of motion. The initial nuclear conditions are obtained from sampling from the Wigner function as in Eq. (13) for all approximate methods here. The propagation of electronic DOFs, $(\mathbf{q}, \mathbf{p})$, was achieved by using the fourth-order explicit Runge–Kutta algorithm, and the nuclear DOF, $(\mathbf{R}, \mathbf{P})$, were propagated by the velocity Verlet integrator with time step Δt summarized in Table III. To improve the accuracy of integration, the electronic time step δt was chosen to be smaller than nuclear Δt such that $20\delta t = \Delta t$. The nonadiabatic dynamics results of these mapping dynamics methods were obtained by averaging over 10^4–10^6 trajectories, and the total averaged trajectories for different models are summarized in Table III. The convergence of the approximate results concerning the time step and number of trajectories has been checked. The ZPE parameter γ was chosen to be method specific: all five versions of LSC dynamics use $\gamma = 1/2$, SQC-square uses $\gamma = 0.366$, SQC-triangle uses $\gamma = 1/3$, SPM-W uses $\gamma = (\sqrt{F+1} - 1)/F$, SPM-P uses $\gamma = 1$, SPM-Q uses $\gamma = 0$, MMST uses $\gamma = 1/2$, and eCMM uses $\gamma = -0.2$. An adiabatic FSSH algorithm is utilized to approximate dynamics of Tully's model. Nuclear propagation used the velocity-Verlet algorithm, mapping variables are propagated using the second-order Verlet algorithm, and nuclear variables share the same updating frequency as mapping variables, $\delta t = \Delta t$. Except for aforementioned simulation details, the adiabatic FSSH shares the same simulation parameters as its diabatic counterpart.

The computational costs for the approximate dynamical methods are summarized in Table S6, for example, the mapping dynamics of a spin-boson model averaged over 10^5 trajectories typically cost from 1.0 to 8.1 core-hours with Intel Xeon Gold 6132 CPU with 2.6 GHz base frequency, and other approximate dynamics nearly scales with the number of trajectories averaged. For the TT calculation, the computational cost heavily depends on the parameters chosen, including the number of basis, TT-rank, and time step, which in turn depends on the specific model. A typical range of computational cost for TT-TFD of spin-boson models is from 4.75 to 12 940 core-hours with dual Intel Xeon Gold 6132 CPU as shown in Table S7.

We note that the focus of the current work is the numerical performance of the approximate dynamical methods, rather than their theoretical rigor when they were proposed. For example, even if the Ehrenfest mean-field method can be rigorously derived, its accuracy cannot be automatically guaranteed. In addition, despite SQC windowing choice being ad hoc, its performance is decent in several cases tested here. The LSC series can be rigorously derived by linearizing the real-time path integral expression of TCF and is capable of capturing important but not all the nuclear quantum effects (NQEs). The accuracy of LSC mapping dynamics depends on using the resolution of identity tricks and the specific choices on the mapping strategies for the electronic operators. The Wigner initial nuclear sampling is naturally derived in LSC, but the original MQC methods were prescribed with classical sampling. To facilitate a direct comparison of methods, we utilized Wigner sampling in all approximate methods studied here. Still, it is important to point out

TABLE III. Simulation parameters of nonadiabatic semiclassical and quasiclassical dynamics of different models, including time step (Δt) of nuclear DOF and the number of trajectories averaged (N_{traj}) for MQC dynamics (Ehrenfest and FSSH), LSC mapping dynamics, and other mapping dynamics.

Models	Δt	N_{traj}(MQC)	N_{traj}(LSC)	N_{traj}(else)
Spin-boson Nos. 1–4,9	$0.001\hbar/\Gamma$	10^4	10^6	10^5
Spin-boson Nos. 5–8	0.001 ps	10^4	10^6	10^5
Fulvene	1×10^{-6} ps	10^4	10^6	10^5
BMA	5×10^{-6} ps	10^4	10^6	10^5
MIA	5×10^{-6} ps	10^4	10^6	10^5
SAC	1×10^{-6} ps	10^4	10^6	10^5
DAC	1×10^{-6} ps	10^4	10^6	10^5
LCP	0.001 a.u.	10^4	10^6	10^5
Retinal	1×10^{-5} ps	10^4	10^6	10^5

that the accuracy of the MQC methods might be improved by using Wigner sampling that essentially captures some static NQE. In addition, in the eCMM method, any ZPE parameter $\gamma \in (-1/F, \infty)$ can be chosen, but the optimal value of γ may vary with the model.

B. Tensor-train based calculations

For all tensor-train-based calculations, convergence tests were performed to ensure the population dynamics results converged to the quantum exact ones. The variables for the convergence test include the time step (Δt), TT-rank, and number of basis functions,

as listed in Table IV. We performed the convergence tests by calculating population dynamics with these three parameters varied and concluded that the results are converged when the changes in population dynamics are no longer observed with added computational cost. We found that all three variables are highly system-dependent. The time step for the spin-boson models was set as $\Delta t = 0.0036\hbar/\Gamma$ for models No. 1–4 and $\Delta t = 10$ a.u. for models No. 5–8. For the LVC models, a time step of $\Delta t = 0.5$ a.u. $= 0.012$ fs was used, and for the retinal model, the time step was set as $\Delta t = 2.5$ a.u. $= 0.0301$ fs. For the spin-boson models and the LVC models, the wavefunctions in the TT-KSL method and thermal wavepacket in the TT-TFD

TABLE IV. Tensor-train-based method and convergence parameters for different models.

Model	Method	Temperature	Time step Δt	TT-rank	Basis[a]	No. of basis[b]	Grid span[c]
Spin-boson No. 1	TT-KSL	0	$0.0036\,\hbar/\Gamma$	20	osc	25	$\cdots$
Spin-boson No. 1	TT-TFD	$0.2\,\Gamma/k_B$	$0.0036\,\hbar/\Gamma$	20	osc	25	$\cdots$
Spin-boson No. 1	TT-TFD	$2\,\Gamma/k_B$	$0.05\,\hbar/\Gamma$	80	osc	25	$\cdots$
Spin-boson No. 2	TT-KSL	0	$0.0036\,\hbar/\Gamma$	20	osc	25	$\cdots$
Spin-boson No. 2	TT-TFD	$0.2\,\Gamma/k_B$	$0.0036\,\hbar/\Gamma$	20	osc	25	$\cdots$
Spin-boson No. 3	TT-KSL	0	$0.0036\,\hbar/\Gamma$	20	osc	25	$\cdots$
Spin-boson No. 3	TT-TFD	$0.2\,\Gamma/k_B$	$0.0036\,\hbar/\Gamma$	20	osc	25	$\cdots$
Spin-boson No. 3	TT-TFD	$2\,\Gamma/k_B$	$0.0125\,\hbar/\Gamma$	115	osc	25	$\cdots$
Spin-boson No. 3	TT-TFD	$10\,\Gamma/k_B$	$0.00625\,\hbar/\Gamma$	90	osc	25	$\cdots$
Spin-boson No. 4	TT-KSL	0	$0.0036\,\hbar/\Gamma$	20	osc	25	$\cdots$
Spin-boson No. 4	TT-TFD	$0.2\,\Gamma/k_B$	$0.0036\,\hbar/\Gamma$	20	osc	25	$\cdots$
Spin-boson No. 5	TT-KSL	0	10 a.u.	20	osc	25	$\cdots$
Spin-boson No. 5	TT-TFD	300 K	10 a.u.	150	osc	25	$\cdots$
Spin-boson No. 6	TT-KSL	0	10 a.u.	20	osc	25	$\cdots$
Spin-boson No. 6	TT-TFD	300 K	10 a.u.	140	osc	25	$\cdots$
Spin-boson No. 7	TT-KSL	0	10 a.u.	20	osc	25	$\cdots$
Spin-boson No. 7	TT-TFD	300 K	10 a.u.	150	osc	25	$\cdots$
Spin-boson No. 8	TT-KSL	0	10 a.u.	20	osc	25	$\cdots$
Spin-boson No. 8	TT-TFD	300 K	10 a.u.	160	osc	25	$\cdots$
Spin-boson No. 9	TT-KSL	0	$0.1\,\hbar/\Gamma$	20	osc	25	$\cdots$
Spin-boson No. 9	TT-TFD	$0.2\,\Gamma/k_B$	$0.1\,\hbar/\Gamma$	20	osc	25	$\cdots$
Spin-boson No. 9	TT-TFD	$2\,\Gamma/k_B$	$0.1\,\hbar/\Gamma$	40	osc	25	$\cdots$
Spin-boson No. 9	TT-TFD	$10\,\Gamma/k_B$	$0.1\,\hbar/\Gamma$	120	osc	25	$\cdots$
Fulvene	TT-KSL	0	0.5 a.u.	40	osc	40	$\cdots$
Fulvene	TT-TFD	300 K	0.5 a.u.	40	osc	40	$\cdots$
BMA	TT-KSL	0	0.5 a.u.	40	osc	45	$\cdots$
BMA	TT-TFD	300 K	0.5 a.u.	40	osc	45	$\cdots$
MIA	TT-KSL	0	0.5 a.u.	45	osc	45	$\cdots$
MIA	TT-TFD	300 K	0.5 a.u.	45	osc	45	$\cdots$
SAC $P_0 = 5$	SOFT	0	4 a.u.	$\cdots$	pos	1024	$[-15, 15)$
SAC $P_0 = 10$	SOFT	0	2 a.u.	$\cdots$	pos	1024	$[-15, 15)$
SAC $P_0 = 20$	SOFT	0	1 a.u.	$\cdots$	pos	1024	$[-15, 15)$
DAC $P_0 = 5$	SOFT	0	2 a.u.	$\cdots$	pos	1024	$[-15, 15)$
DAC $P_0 = 15$	SOFT	0	2 a.u.	$\cdots$	pos	1024	$[-15, 15)$
DAC $P_0 = 30$	SOFT	0	1 a.u.	$\cdots$	pos	1024	$[-15, 15)$
LCP	SOFT	0	0.001 a.u.	$\cdots$	pos	2048	$[-30, 30)$
Retinal	TT-SOKSL	0	2.5 a.u.	70	pos	$256/32\ (\theta/R)$[d]	$[-\pi, \pi)/[-5, 5)$

[a]"osc" indicates the occupation number basis of a harmonic oscillator, and "pos" indicates the position grid basis.
[b]Number of basis refers to the maximum occupation number when used with "osc" and the number of grid points when used with "pos."
[c]The range of spatial basis in the atomic unit for SOFT simulation.
[d]For the retinal model, 256 grid points in the position basis are used for the rotational mode and 32 grid points are used for the rest harmonic modes.

method [Eq. (45)] are expanded by the harmonic oscillator eigen-basis. Due to the high proximity of the spin-boson model to the harmonic oscillator, ten basis functions are usually sufficient for the convergence of population dynamics. However, for the sake of consistency, we performed simulations on spin-boson models all with a basis size of 25. For the convergence of TT-rank on the spin-boson models, TT-TFD poses a slightly higher requirement than TT-KSL due to the added entanglement between the system and fictional components of the thermal wavepacket. The LVC models have more complexity than the spin-boson models by including electronic coupling terms that are linear to vibrational modes, among which the most demanding TT-TFD for MIA model required a TT-rank of 45 and 45 harmonic eigenbasis. Meanwhile, for the more complicated retinal model, a dense position grid was used to expand the wavefunction due to the highly anharmonic nature of the retinal primary reactive mode. The primary mode requires at least 200 spatial grid points to converge, and the TT-rank would converge at around 70. The TT-TFD results of spin-boson models No. 1–4 at $\beta = 5$ have been confirmed to agree with the numerically exact QuAPI results,[69,109] and the TT-KSL results of spin-boson models No. 5–8 at zero temperature have been confirmed to agree with numerically exact ML-MCTDH.[104]

In the SOFT method for Tully's models, grid points of 256 in the position basis are usually sufficient and we used 1024 position grid points to ensure a great convergence. The time step in SOFT propagation varies for different kinetic energies, and higher initial momentum usually requires smaller Δt. For the SAC model, in the $P_0 = 5$ case, $\Delta t = 4$ a.u. is sufficient; in the $P_0 = 15$ case, $\Delta t = 2$ a.u. is proper; and in the $P_0 = 30$ case, $\Delta t = 1$ a.u. is required. For the DAC model, in the $P_0 = 5$ case, $\Delta t = 4$ a.u. is sufficient; in the $P_0 = 15$ case, $\Delta t = 2$ a.u. is proper; and in the $P_0 = 30$ case, $\Delta t = 1$ a.u. is required. Grid points in the position basis are placed in an equally spaced manner, and the first point is located at the left limit of the grid span. For the LCP model, time step $\Delta t = 0.001$ a.u., and 2048 grid points are utilized for convergence.

V. RESULTS AND DISCUSSION

A. Nonadiabatic dynamics with spin-boson models

The spin-boson model is one of the most widely used models for understanding nonadiabatic dynamics in condensed-phase systems. A faithful prediction of its electronic dynamics is key for testing quantum dynamical methods that could be potentially useful for large and complex condensed phases. The spin-boson model features harmonic PES and Condon (constant) electronic coupling, which are decent approximations for condensed phase systems. Here, we consider eight spin-boson models that correspond to a range of thermodynamic energetic driving force, reorganization energy, and electronic coupling, and the key model parameters are summarized in Table I.

The population dynamics of spin-boson model No. 1 in terms of the population difference between the donor state and the acceptor state, i.e., $\sigma_z(t) = \sigma_{DD}(t) - \sigma_{AA}(t)$, are reported in Fig. 1. Spin-boson model No. 1 has a biased energy offset ($\epsilon = 1.0$) and a small reorganization energy ($E_r = 0.198$) compared with electronic coupling $\Gamma = 1.0$), which is expected to have very oscillatory population dynamics. It is evident that the population oscillations are more significant at $k_B T = 0$ (upper panels of Fig. 1) than at $k_B T = 0.2$
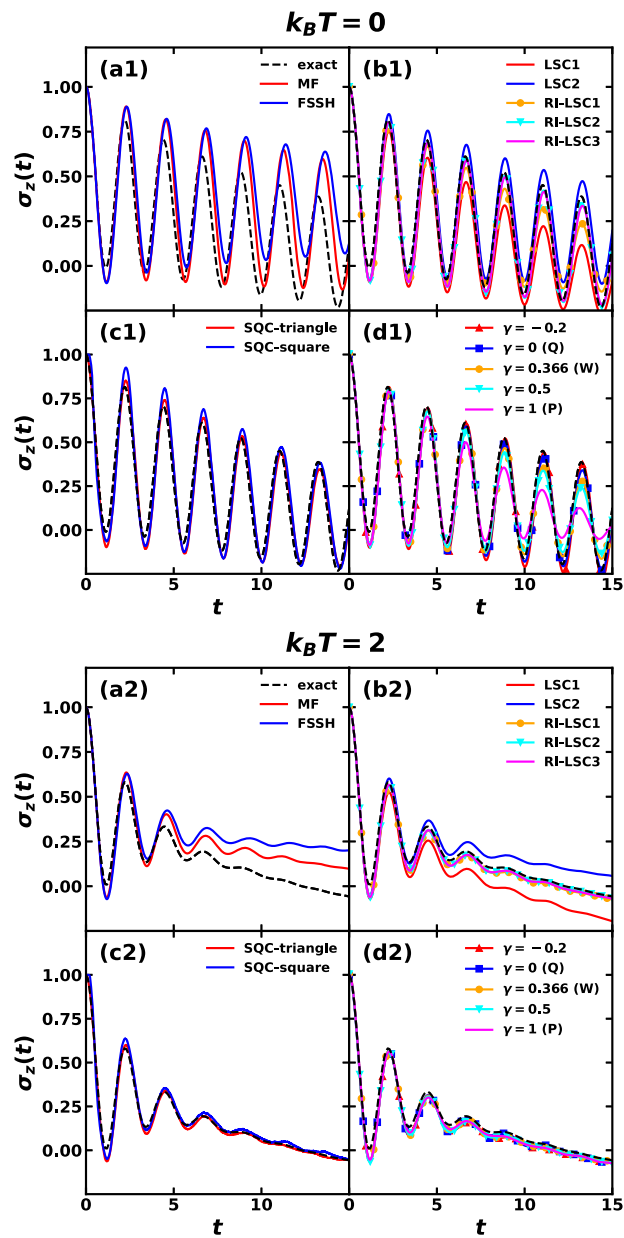

FIG. 1. Population difference dynamics of spin-boson model No. 1 at zero temperature (upper panels) and at $k_B T = 2$ (lower panels) obtained with various approximate mixed quantum–classical, semiclassical, and quasiclassical dynamics methods (solid lines) in comparison with numerically exact dynamics at zero temperature by TT-KSL and at finite-temperature by TT-TFD (dashed line).

(lower panels of Fig. 1), which can be attributed to the thermal damping due to the broader nuclear distribution at a higher temperature. First, MQC methods, including Ehrenfest and FSSH, seem able to capture only the general oscillatory trend but not the amplitude and phase quantitatively, compared with the numerically exact TT-SOKSL dynamics for zero temperature and TT-TFD dynamics

for finite temperature [Figs. 1(a1) and (a2)]. Second, the five LSC mapping dynamics give better agreement with the exact results than MQC methods [Figs. 1(b1) and 1(b2)]. Here, LSC1 and LSC2 can capture the oscillation phase, but underestimate and overestimate the population oscillation, respectively. In contrast, the population oscillation is well reproduced when the RI trick for the identity operator is employed in RI-LSC1–3 methods, especially since the exact result can be accurately reproduced by RI-LSC2 and RI-LSC3 approaches. Third, the SQC dynamics give an excellent agreement with the exact population dynamics, where the SQC with triangle window function behaves better than the square window function by having a smaller oscillation amplitude [Figs. 1(c1) and 1(c2)]. Fourth, the eCMM/SPM approaches are seen to capture the oscillation phase of population accurately, and the oscillation amplitude shows an anticorrelation with the ZPE parameter: the amplitude grows to better match the exact result when decreasing γ values from 1 (P scheme), 0.5, 0.366 (W scheme), 0 (Q scheme), and −0.2 [Figs. 1(d1) and 1(d2)]. We are not expecting that different ZPE parameter choices, including P, Q, W schemes of SPM, would lead to the similar accuracy; instead, the best eCMM/SPM method for the tested spin-boson models is when a negative ZPE parameter is chosen $\gamma = -0.2$. In short, among all the approximate methods taken into consideration, we found that RI-LSC2, RI-LSC3, SPM-Q/eCMM with $\gamma = 0$, and eCMM with $\gamma = 0$–0.2 can generate the best match with the exact result for spin-boson model No. 1.

In Fig. 2, we show the population dynamics of spin-boson model No. 3. This model has a larger reorganization energy ($E_r = 1.488$) than spin-boson model No. 1; thus, spin-boson model No. 3 displays a more damped oscillation in the population difference between donor and acceptor states than spin-boson model No. 1 does (Fig. 1) as expected since the reorganization energy depicts the strength of electronic-nuclear coupling. The zero-temperature ($k_BT = 0$) and the finite-temperature ($k_BT = 0.2$) dynamics obtained with the same method are very similar, which can be traced back to the fact that the Wigner initial sampling widths at the finite temperature [Eq. (53)] are close to those at zero temperature [Eq. (54)] for those high-frequency modes due to high ω_c and ω_{max} values. The exact result of spin-boson model No. 3 seems more challenging to reproduce than spin-boson model No. 1, for example, the traditional MQC methods of Ehrenfest and FSSH fail to predict the population dynamics except for the very short time [Figs. 2(a1) and 2(a2)]. Among the LSC methods, LSC1 underestimates the population decay and LSC2 overestimates the population decay again as in the previous model, and the RI versions give much better population dynamics, of which RI-LSC3 offers the best prediction for σ_z [Figs. 2(b1) and 2(b2)]. The two SQC approaches generate almost the same result, but the long-time oscillation in population is not captured [Figs. 2(c1) and 2(c2)]. In contrast, the eCMM/SPM method shows a trend of systematic improvement in the population dynamics when decreasing the ZPE parameter, and eCMM/SPM $\gamma = 0$ (Q scheme) and $\gamma = -0.2$ are found to produce the optimal agreement with the reference result [Figs. 2(d1) and 2(d2)]. Thus, for spin-boson model No. 3, RI-LSC2, RI-LSC3, SPM-Q/eCMM with $\gamma = 0$, and eCMM with $\gamma = 0$–0.2 seem to provide accurate population dynamics compared with the numerically exact result.

Furthermore, the coherence dynamics of spin-boson model No. 3 is shown in Fig. 3. Like population dynamics, MQC methods, such as Ehrenfest and FSSH, fail to accurately capture the coherence
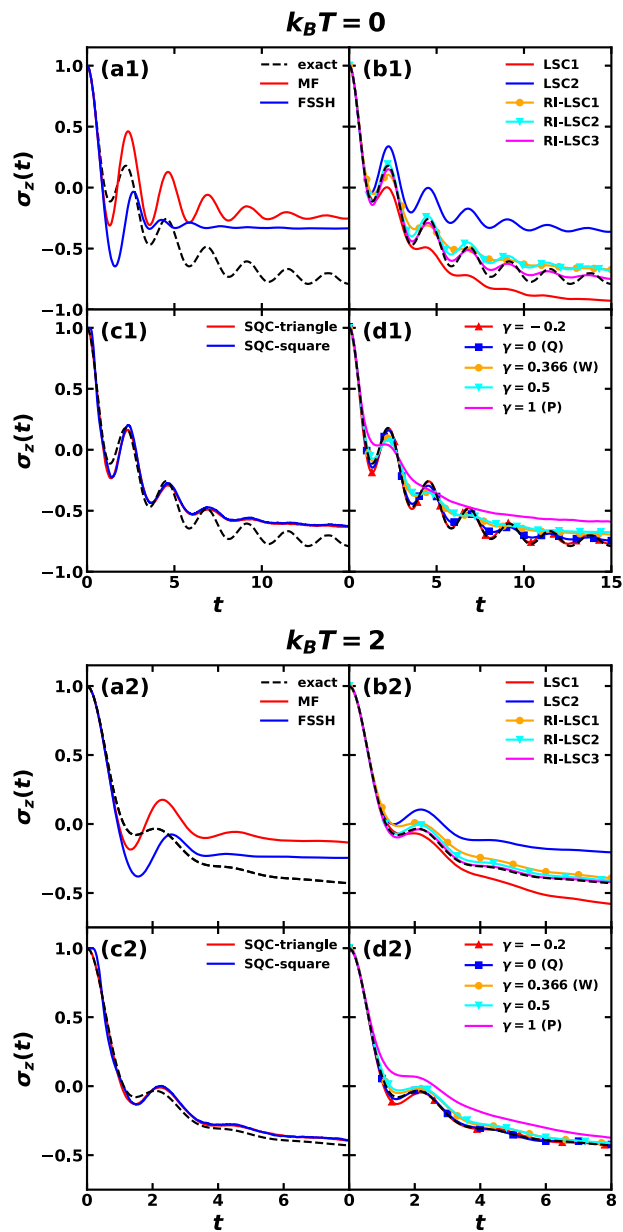

FIG. 2. Population difference dynamics of spin-boson model No. 3 at zero temperature (upper panels) and at $k_BT = 2$ (lower panels) obtained with various approximate mixed quantum–classical, semiclassical, and quasiclassical dynamics methods (solid lines) in comparison with numerically exact dynamics at zero temperature by TT-KSL and at finite-temperature by TT-TFD (dashed line).

dynamics. Ehrenfest dynamics averages over quantum states, which disrupts the accurate representation of quantum superpositions and thus their coherence, while the original FSSH lacks explicit decoherence treatment. LSC methods provide better coherence dynamics than MQC methods, accurately reproducing the oscillation phase of both the real and imaginary parts of the coherence. Among these, LSC methods with RI treatment appear to perform particularly well.
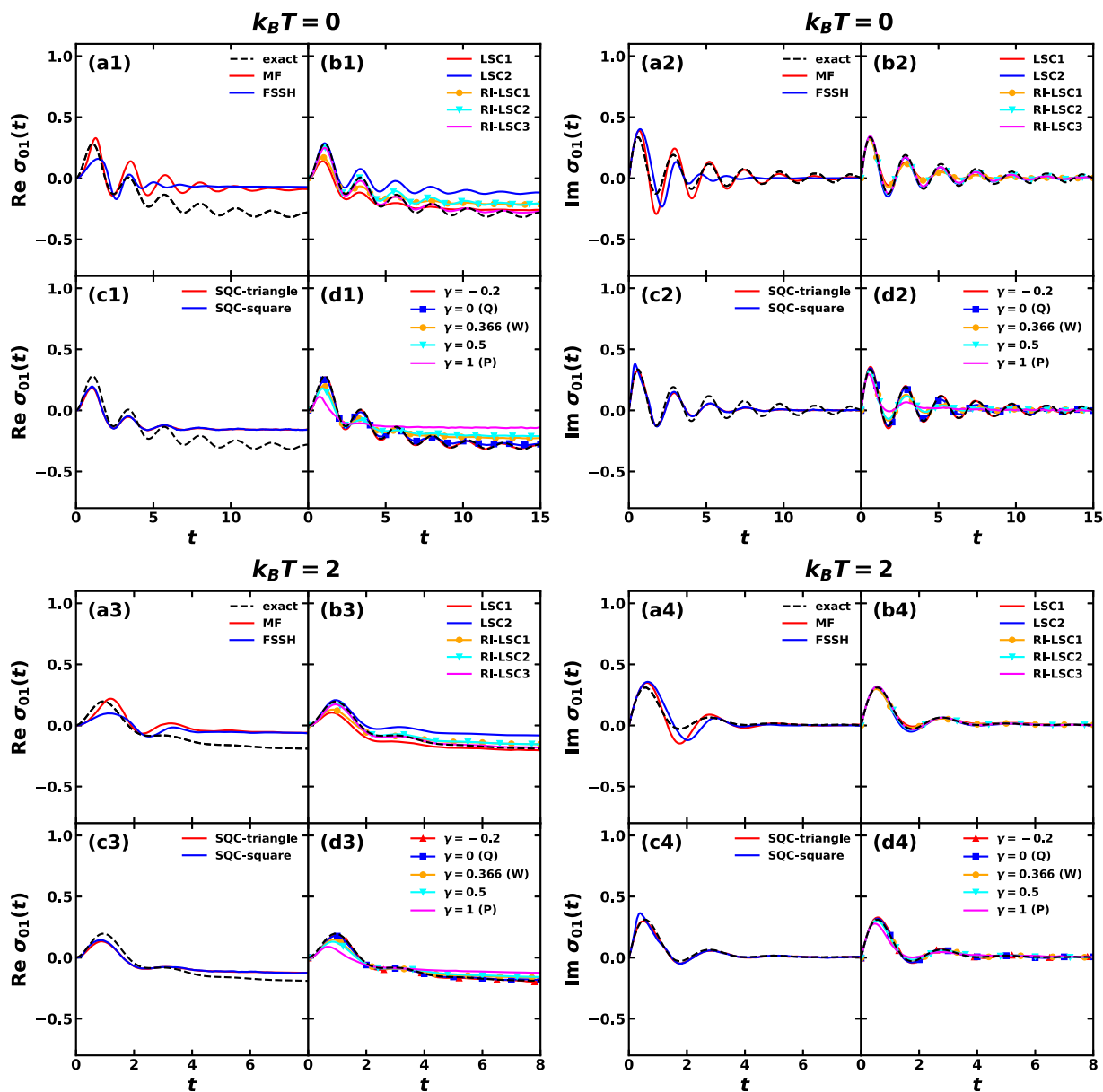
FIG. 3. Coherence dynamics of spin-boson model No. 3 at zero temperature (upper panels) and at $k_B T = 2$ (lower panels) obtained with various approximate mixed quantum–classical, semiclassical, and quasiclassical dynamics methods (solid lines) in comparison with numerically exact dynamics at zero temperature by TT-KSL and at finite-temperature by TT-TFD (dashed line). The real and imaginary parts of $\sigma_{01}(t)$ are plotted in the left and right panels, respectively.

The SQC methods with triangle and square windows seem to behave identically and exhibit overdamped coherence, attributed to the inherent broadening effects of these window functions. The eCMM methods with $\gamma = -0.2$ and $\gamma = 0$ (SPM-Q) show the best agreement with the exact coherence dynamics among all approximate methods tested.

We show other spin-boson models' comparison between approximate and exact dynamical methods in the supplementary material, where the population dynamics of spin-boson models No.

1–No. 9 at different temperatures are plotted in Figs. S1–S9 and the coherence dynamics of spin-boson models No. 1, No. 2, and No. 4 are shown in Figs. S10–S12. Generally, for all spin-boson models tested here, the traditional MQC methods, including Ehrenfest and FSSH, give the worst prediction to the population dynamics and even cannot capture the phase of the population oscillation. LSC1 and LSC2 tend to underestimate and overestimate the population difference, respectively, while LSC with RI trick gives a much better prediction, in which RI-LSC1 often has a smaller oscillation

amplitude than RI-LSC2 and RI-LSC3. SQC-triangle gives similar results as SQC-square, except for very early time square window might produce incorrect flat population dynamics due to the finite window width. SPM-Q and eCMM with negative ZPE parameters tend to give better agreement with the exact result for oscillatory population dynamics. The root-mean-square errors of the approximate methods from the exact results for all spin-boson models considered here are summarized in Table S5. For the coherence dynamics, similar performance can be observed that the LSC with RI treatment, eCMM with $\gamma = 0$ (SPM-Q), and $\gamma = -0.2$ are generally accurate, and the SQC methods would generate accurate coherence dynamics when they can capture the population dynamics. To sum up, RI-LSC2, RI-LSC3, SQC-triangle, eCMM with $\gamma = 0$ (SPM-Q), and $\gamma = -0.2$ are seen to provide excellent agreement with the exact population dynamics for the spin-boson models.

Some model-specific comments are provided below. Spin-boson model No. 2 shown in Fig. S2 has a biased energy offset and intermediate reorganization energy; thus, the population dynamics are expected to be in between models No. 1 and No. 3, where we observe intermediately oscillatory population decay and more damped oscillation at a higher temperature than at zero temperature, and the optimal dynamical method choices for model No. 2 are RI-LSC2,3 and SPM-Q/eCMM ($\gamma = 0$). Spin-boson model No. 4 shown in Fig. S4 has an unbiased energy offset and intermediate reorganization energy; thus, the population difference is expected to vanish in the long-time limit after a few damped oscillation periods, which is observed, and the best method for this model is eCMM ($\gamma = -0.2$) with the largest oscillation amplitude.

Spin-boson models No. 5–No. 8 have the same biased energy offset ($\epsilon = 50$ cm^{-1}) but different electronic couplings and reorganization energies. Spin-boson models No. 5 and No. 6 shown in Figs. S5 and S6, respectively, have a small electronic coupling ($\Gamma = 20$ cm^{-1}), model No. 5 has a small reorganization energy, and model No. 6 has a large reorganization energy. Both of the models display an overdamped population decay, especially a monotonic decay as seen in model No. 6. The population dynamics at zero temperature can be better captured by semiclassical dynamics methods than the population dynamics at finite temperature in both models No. 5 and No. 6, and the growing deviation between approximate dynamics and TT-TFD dynamics at 300 K at a long time seems to require double checking with another numerical exact method. In addition, the SQC-square method does not show population decay at the early time compared with the exact results, and in contrast, SQC-triangle does not suffer from this deviation. This phenomenon can be attributed to the fact that different window shapes and sizes affect the determination of the population of a particular state: the square windows with $\gamma = 0.366$ have a gap between two electronic states, whereas the triangle windows with $\gamma = 1/3$ contact at the vertices, and thus, SQC-square is seen to have a delay in population transfer, whereas SQC-triangle does not. Spin-boson models No. 7 and No. 8 shown in Figs. S7 and S8, respectively, have a large electronic coupling ($\Gamma = 100$ cm^{-1}), model No. 7 has a small reorganization energy, and model No. 8 has a large reorganization energy. Both of the models display underdamped population dynamics, especially a less oscillatory profile as seen in model No. 8 with a large reorganization energy of about $E_r = 200$ cm^{-1}. An interesting rephasing phenomenon corresponding to a regaining of population oscillation amplitude is observed in models No. 7 and No. 8. This can be

better understood by increasing the number of modes in the TT-based exact dynamics as depicted in Fig. S13, where models No. 7 and No. 8 with $N = 60$ modes show significant rephasing but the same models No. 7 and No. 8 with $N = 250$ modes do not. Although the rephasing feature is less likely to happen in the condensed-phase
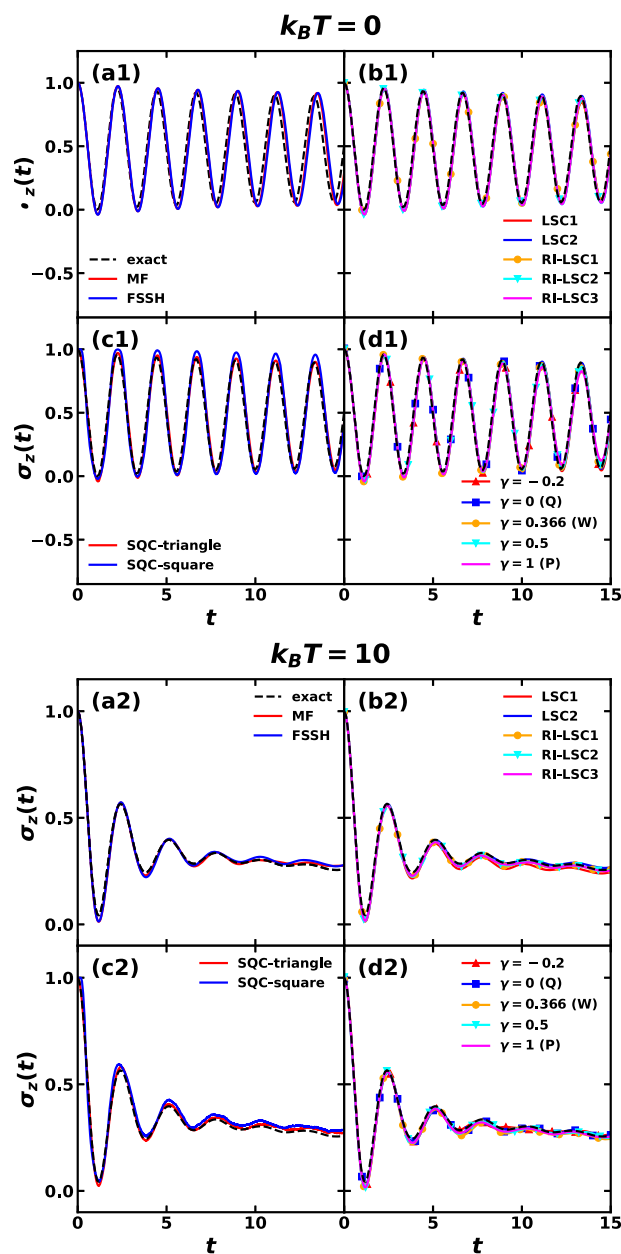

FIG. 4. Population difference dynamics of spin-boson model No. 9 at zero temperature (upper panels) and at $k_BT = 10$ (lower panels) obtained with various approximate mixed quantum–classical, semiclassical, and quasiclassical dynamics methods (solid lines) in comparison with numerically exact dynamics at zero temperature by TT-KSL and at finite-temperature by TT-TFD (dashed line).

limit with a large number of modes, the semiclassical and quasiclassical methods seem unable to capture this feature when the number of modes is limited.

In Fig. 4, we show a much more friendly spin-boson model No. 9, where almost all approximate methods agree with the exact results well at temperatures $k_BT = 0$ and $k_BT = 10$, except for a slight out-of-phase deviation seen in MQC methods. An important feature of this model is the small reorganization energy ($E_r = 0.080$) compared with the electronic coupling ($\Gamma = 1.0$) and the energy offset ($\epsilon = 1.0$). This model is also easy to get numerically exact results with the tensor-train approaches, and the time step can be relatively large ($\Delta t = 0.1\hbar/\Gamma$) compared with other spin-boson models. Similarly, in Fig. S9, it is evident that all approximate methods demonstrate excellent agreement with the exact results at $k_BT = 0.2$ and $k_BT = 2$. Model No. 9 is expected to alleviate the stress experienced by our readers resulting from the complexities observed in the more challenging spin-boson models No. 1–8.

B. Electronic transition through conical intersections with LVC models

The non-Condon effect arises when the electronic coupling is no longer a constant but dependent on nuclear configuration, and such an effect would be important for understanding electronic transition through conical intersections and long-range electron transfer. To this end, we report the benchmark test for fulvene, BMA, and MIA molecules that are described by LVC model Hamiltonians with electronic couplings linearly dependent on the coordinates. These gas-phase molecular systems would be particularly more challenging to simulate than condensed-phase systems, for the reason that the molecular vibrational modes, the electronic-nuclear couplings, and the off-diagonal electronic couplings may be more structured than the condensed-phase case. These LVC models have been benchmarked for the LSC and SQC dynamics at zero temperature,[89] but not at finite temperature, and also were not tested with SPM/eCMM methods before.
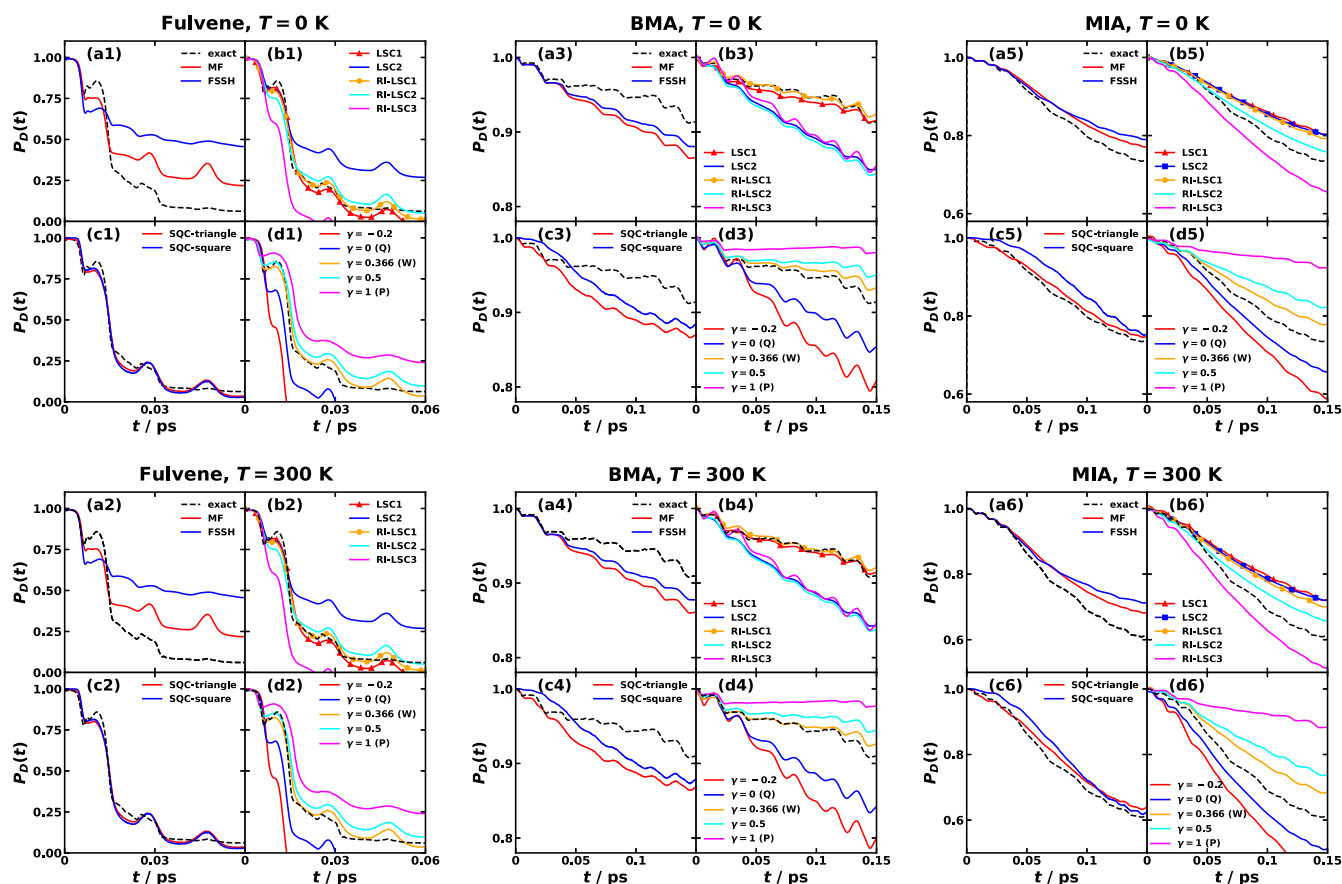

FIG. 5. Electronic transition through conical intersections in fulvene (left), BMA (middle), and MIA (right) molecules at zero temperature (upper) and $T = 300$ K (lower) obtained with various approximate and numerically exact methods. The donor state population of linear vibronic coupling (LVC) models of the three molecules is plotted as a function of time with the initial state described in Table II. The numerically exact dynamics at zero temperature and finite temperature are computed with TT-KSL and TT-TFD, respectively (dashed), which is compared with mixed quantum–classical, semiclassical, and quasiclassical dynamics methods.

In Fig. 5, we show the combined results for fulvene, BMA, and MIA at zero temperature as well as at the finite temperature of 300 K. First, the population decay in fulvene exhibits a similar signature stepwise pattern in both zero temperature and finite temperature cases, and most of the donor state population is transferred to the acceptor state in ultrafast time scale (0.03 ps) (left panels of Fig. 5). MQC methods of Ehrenfest and FSSH, as well as LSC2, SPM/eCMM with $\gamma = 1$ (P scheme), and $\gamma = 0.5$, tend to underestimate the population decay, whereas RI-LSC3, SPM/eCMM with $\gamma = 0$ (Q scheme), and $\gamma = -0.2$ tend to overestimate the population decay, leading to an unphysical negative population in a long time. Excellent agreement with the exact dynamics can be found with RI-LSC1, RI-LSC2, LSC1, SQC-square, SQC-triangle, and SPM/eCMM with $\gamma = 0.366$ (W scheme), and the best agreement is seen with RI-LSC1 for fulvene. Second, in the BMA case, the best agreement with exact dynamics is found to be RI-LSC1 again, the excellent agreement can be produced with LSC1 and SPM/eCMM with $\gamma = 0.366$ (W scheme), and the rest methods display significant error. Third, in the MIA case, we observe a faster population decay at 300 K than at zero temperature and MIA with the largest number of modes shows a smoother decay profile in contrast to the above-mentioned two cases. The best agreement with exact dynamics in MIA is achieved with SQC-triangle dynamics, while other methods tend to have large errors. To sum up, the electronic transition through conical intersections in the three gas-phase molecules can be captured accurately with SQC-triangle for MIA and RI-LSC1 for fulvene and BMA.

C. Photoisomerization of retinal

The 25-mode photoisomerization model of retinal from rhodopsin visual system consists two primary modes, including the anharmonic *cis-trans* torsion coordinate $\hat{\theta}$ and the linear coupling harmonic mode $\hat{R}_c$, and these primary modes are coupled to 23 bath modes. The electronic coupling is linearly dependent on $\hat{R}_c$, which accounts for the non-Condon effect. With anharmonic potential and non-Condon coupling, the retinal photoisomerization model emerges as one of the most challenging types of model to test. Besides the above-mentioned semiclassical dynamics methods, we added a few dynamics with focused initial sampling for the mapping variables to this model for better nuclear dynamics. The retinal molecule is initially photoexcited to the excited state (S_1) and in the *cis* isomer; then, the electronic population gets transferred to the ground state (S_0) and the nuclear structure evolves to gain *trans* isomer fraction in the picosecond timescale. Figure 6 shows both electronic population dynamics (upper panels) and nuclear isomerization dynamics (lower panels) of photoexcited retinal at zero temperature where the numerically exact result was obtained with TT-SOKSL. Finite-temperature calculation of this model is difficult since the Wigner transformed distribution of the rotational degree of freedom is too wide even at 4 K to converge tensor networks numerically. Electronic population dynamics is reported as the ground state (S_0) population as a function of time, and the exact quantum mechanical dynamics shows features including that the initial rise in population starts at about 0.1 ps after a few small-amplitude Rabi oscillations, the first peak around ground state population of 0.5 is reached at 0.3 ps, then a slight decay is seen during $t = 0.25-0.4$ ps, and subsequently the ground state population is slowly accumulated
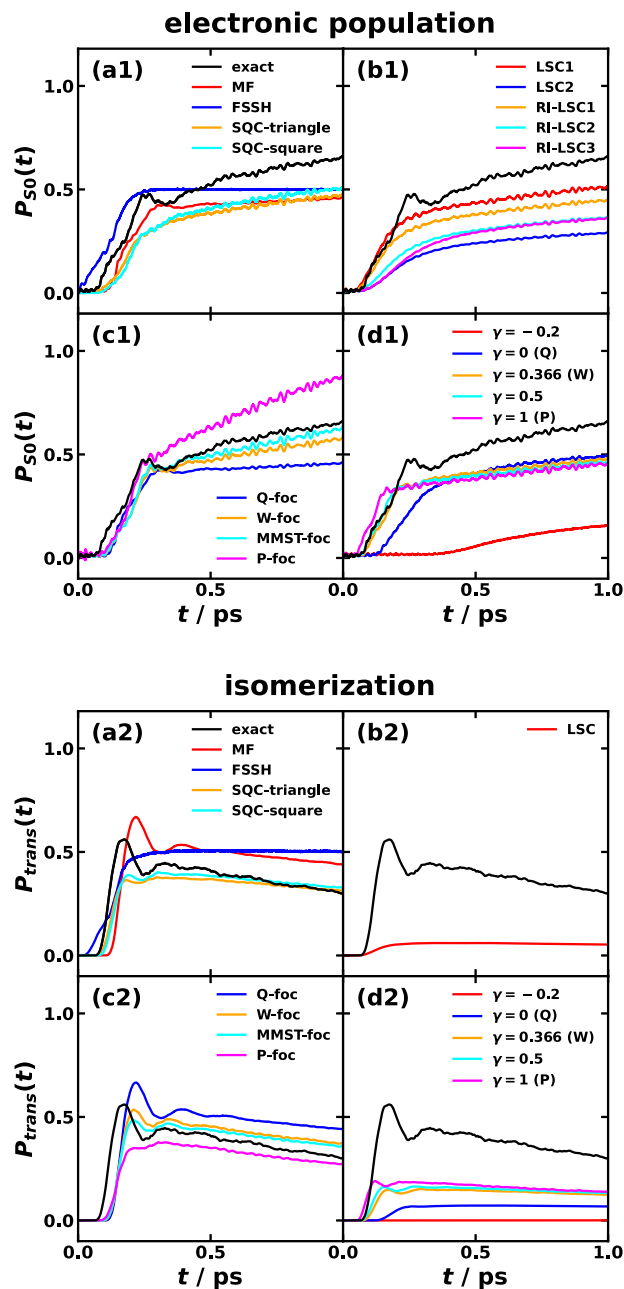

FIG. 6. Photoisomerization dynamics of 25-mode retinal at zero temperature, including the ground electronic state (S_0) population dynamics (upper panels) and the *trans* isomer fraction dynamics (lower panels) after initially photoexcited to the S_1 excited state in the *cis* isomer, as obtained with numerically exact TT-SOKSL and various mixed quantum–classical, semiclassical, and quasiclassical dynamics methods.

to about 0.65 in 1 ps. The signature first peak at around 0.25–0.3 ps and the subsequent growth in ground-state population are seen in W-foc, Q-foc, MMST-foc, and Ehrenfest methods, of which W-foc and MMST-foc produce the most accurate electronic dynamics

compared with the exact result. SQC and LSC methods [Figs. 6(a1) and 6(b1)] fail to capture the first peak and underestimate the population growth, of which LSC1 and RI-LSC1 generate relatively better predictions since they tend to foster population transfer as also seen in the spin-boson models. It is evident that SPM/eCMM methods with sphere sampling of mapping variables systematically underestimate the population growth when compared with the corresponding SPM with focused sampling of mapping variables [Figs. 6(c1) and 6(d1)], and this can be traced back to the fact that the focused sampling would give more concentrated initial nuclear forces from the PES of the initially populated electronic state, which would drive the system away from the reactant region. The FSSH, LSC2, RI-LSC2/3, P-foc, and SPM/eCMM ($\gamma = -0.2, 0$) barely capture the qualitative trend of the electronic dynamics, where the worst method is eCMM ($\gamma = -0.2$).

The isomerization reaction is characterized by the *cis–trans* dihedral angular nuclear dynamics as displayed in Figs. 6(a2)–6(d1). The exact result by TT-SOKSL shows that the first peak for the *trans* isomer fraction of 0.55 is reached at $t = 0.2$ ps, the second peak of about 0.45 *trans* fraction is reached at $t = 0.3$ ps, and then, the *trans* fraction decays gradually to about 0.3 at $t = 1$ ps. The best nuclear dynamics are reproduced by W-foc and MMST-foc methods as shown in Fig. 6(c2), where the two-peak signature is seen with a small time delay, which is much more accurate in nuclear dynamics compared with their sphere-sampling counterparts in Fig. 6(d2). The superb performance in generating nuclear dynamics with the W-foc and MMST-foc is because the initial nuclear forces are guaranteed to be determined by solely the PES of the initially populated electronic state when focused sampling of mapping variables is utilized. In contrast, when full sphere sampling of mapping variables is used, such as in SPM/eCMM methods, the initial nuclear forces result from averaging all electronic PESs uniformly, which include the unpopulated electronic state, thus making the nuclear dynamics unphysical, at least for the initial ultrafast timescale. Ehrenfest and Q-foc overestimate the peak height with a 0.5 ps delay, but the main *trans* fraction profile is reproduced. Finally, FSSH, LSC, and SPM/eCMM fail in producing the *trans* fraction profile, and the reason for LSC and SPM/eCMM is that uniform Gaussian sampling or full sphere sampling would lead to unphysical initial nuclear forces, thus hindering the *cis* to *trans* molecular structural change. Considering both electronic and nuclear dynamics, the best approximate methods for retinal with anharmonic potential and non-Condon coupling are W-foc and MMST-foc using focused sampling of mapping variables.

D. Tully's models

Tully's classic models were initially proposed for testing the FSSH method,[107] and here, we test single avoided crossing (SAC) and double avoided crossing (DAC) models, which mimic scattering problems in one dimension. It is noted that both SAC and DAC models have anharmonic potential and non-Condon coupling, but in a low-dimensional nuclear space, which is different from any condensed-phase environment. The DAC model is shown in Fig. 7, where we observe two different nonadiabatic population transfer dynamics with small and large initial momenta. When the initial momentum is small ($p_0 = 5$), a temporary population transfer to
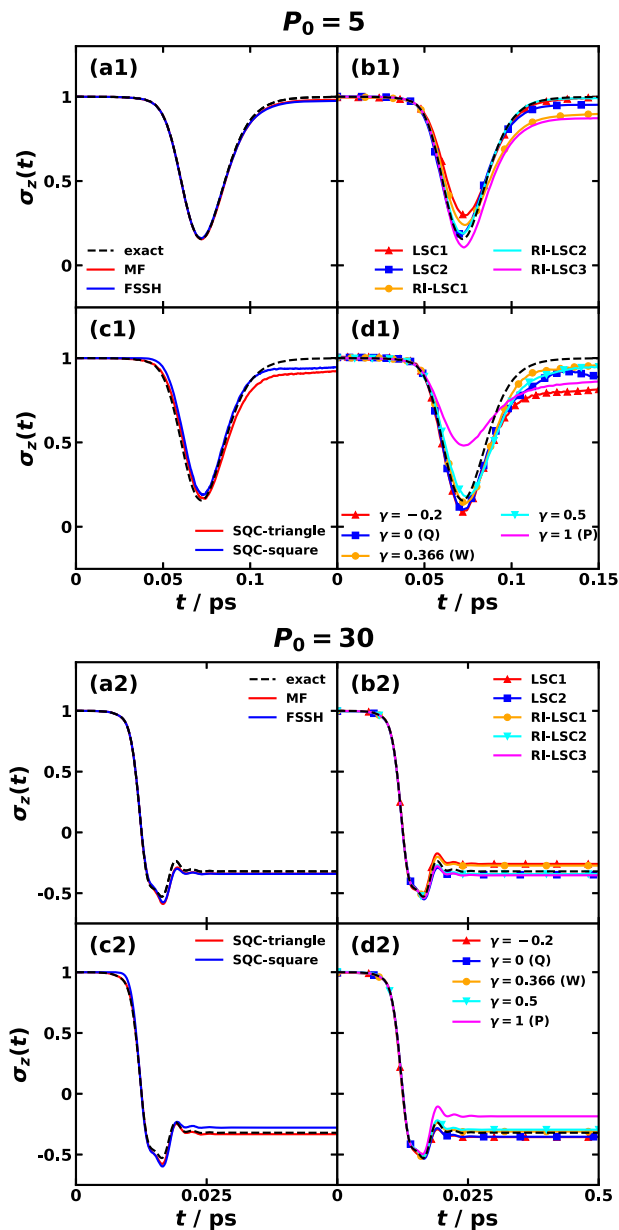

FIG. 7. Nonadiabatic dynamics $\sigma_z(t) = \sigma_{00}(t) - \sigma_{11}(t)$ of Tully's double avoid crossing (DAC) model at zero temperature with low initial momentum $p_0 = 5$ (upper panels) and high initial momentum $p_0 = 30$ (lower panels), where the exact result is obtained with the SOFT method and the approximate results are obtained with various mixed quantum–classical, semiclassical, and quasiclassical dynamics methods.

the other diabatic state occurs during 0.05–0.1 ps; then, the population gets transferred back to the original state. This behavior is well-captured by Ehrenfest, FSSH, RI-LSC2, LSC2, SQC, SPM-W, and eCMM ($\gamma = 1/2$), and relatively large errors are seen with LSC1 and SPM-P methods. When the initial momentum is large ($p_0 = 30$), a permanent population transfer is recognized and most

of the approximate methods can generate the correct dynamics, except for SPM-P, which gives relatively large errors.

The SAC model is shown in Fig. S19, where most of the approximate dynamical methods give correct semiquantitative predictions compared with exact quantum dynamics. The differences between various methods with small initial momentum ($p_0 = 5$) are more significant than those with large initial momentum ($p_0 = 20$). In the case of small initial momentum, accurate results are produced by RI-LSC1, LSC1, LSC2, SQC-square/triangle, SPM-W, and eCMM ($\gamma = 1/2$), and relatively large errors are observed in Ehrenfest, FSSH, RI-LSC2, SPM-P, SPM-Q, and eCMM ($\gamma = -0.2$). In the case of large initial momentum, there are no significant differences among different approximate methods, and they are all quite accurate but do not perfectly reproduce the exact result either. The SAC model with initial momentum $p_0 = 10$ and DAC model with initial momentum $p_0 = 15$ are shown in Figs. S20 and S21, respectively. It is noted that in the current implementation of FSSH, we used the wavefunction expansion coefficients for calculating population, while counting active states that could give better population have been reported in Ref. 110. To sum up, for these one-dimensional Tully's models, most approximate methods would work, and LSC2, SQC, and SPM-W typically provide accurate results. However, we notice that SPM-P is consistently bad in most cases we tested in this study, which might be because the large ZPE parameter may cause temporary flipped PES and thus unphysical forces when $(q_j^2 + p_j^2)/(2\hbar)$ is too small compared with γ.

E. LCP model

The LCP model is a challenging model for semiclassical or mixed quantum–classical methods. This one-dimensional model is far from any multidimensional condensed-phase system, where the semiclassical or mixed quantum–classical approaches tend to give reasonable predictions. Here, we used two vibrational eigenstates of the parabola, including a low-lying case ($n = 15$) and a high-lying case ($n = 30$) as the nuclear initial conditions.

In the low-lying case shown in Fig. S22, the numerically exact result shows a clear change of decay slope around 6 a.u. Although Ehrenfest and FSSH approaches exhibit less deviations from the exact results than the semiclassical mapping approaches, the Ehrenfest method does not capture the change of slope and FSSH gives an opposite slope trend. The LSC, SQC, and SPM methods show larger population deviations from the reference than the MQC methods. In the high-lying case shown in Fig. S23, the numerically exact results show a few oscillations. RI-LSC2 is seen to capture the first and half oscillations, better than the other methods. For the MQC approaches, FSSH gives better results than the Ehrenfest method. In the two tests, we observe that most of the MQC and semiclassical methods falter with this model, except for very early population decay. This failure may stem from inadequacies in the approximate methods for generating effective nuclear forces, which may not even exist in the multistate and extremely anharmonic PESs.

VI. CONCLUDING REMARKS

In this work, we systematically benchmarked various mixed quantum–classical, semiclassical, and quasiclassical dynamics methods in model systems against numerically exact tensor-train-based quantum dynamics methods, including TT-KSL for zero-temperature cases and TT-TFD for finite-temperature cases. Generally speaking, the choice of optimal approximate dynamical methods is a case-by-case problem, and for different natures of models, the answer varies dramatically. For the spin-boson model with harmonic potential and Condon coupling, we found that RI-LSC2/3, SQC-triangle, SPM-Q/eCMM ($\gamma = 0$), and eCMM ($\gamma = -0.2$) could give accurate population dynamics at zero and finite temperatures. For the LVC model of electronic transition through conical intersections parameterized by harmonic potential and non-Condon coupling, SQC-triangle worked the best for the MIA system with a larger number of modes and RI-LSC1 worked the best for fulvene and BMA systems with fewer modes. For the photoisomerization reaction in retinal that is described by anharmonic potential and non-Condon coupling, we found that W-foc and MMST-foc with focused sampling of mapping variables could produce accurate electronic and nuclear dynamics, which is attributed to the accurate initial nuclear forces from the focused sampling on the initial electronic state. For Tully's SAC and DAC scattering problem in one dimension, most approximate dynamical methods would work, such as LSC2, SQC-triangle/square, and SPM-W. It is challenging to capture the exact quantum dynamics in the LCP model using the approximate methods employed here. We note that SPM-P with $\gamma = 1$ consistently produces inaccurate results in most of the tested models and thus is not recommended to use.

There are several future directions based on the current work. The approximate method choice for benchmark could never be complete since many approximate methods emerged in recent years. For example, the partial linearized density matrix (PLDM)[111,112] and spin-PLDM[113,114] are based on treating the forward and backward propagation of electronic reduced density matrix separately and nuclear propagation with full linearization approximation, but it is beyond the current semiclassical and quasiclassical dynamics that share the equation of motion and thus beyond the scope of this work. In addition, quantum dynamics in a more sophisticated multi-state harmonic (MSH) model[14,71] and multi-state reaction coordinate (MRC) model[115] that are constructed from all-atom simulations could be evaluated with the tensor-train-based methods, which in turn pave the way for rational selection of approximate methods to all-atom nonadiabatic dynamics. The TCFs provided by the suitable approximate methods could be directly used for understanding transient electronic transition, such as photoinduced charge and energy transfer in the condensed phase.[116–118] There are also several ways to correct the initial sampling of mapping variables such that the initial nuclear forces are physical, including changing ZPE parameters statically[54] or dynamically.[113,119] When applying nonadiabatic dynamics, it is important to validate the approximate dynamical methods before applying them to more complicated systems where exact results are impossible to get. Benchmark studies have provided and will keep providing practical guidance in simulations of realistic nonadiabatic processes in complex condensed phases, such as organic photovoltaics, luminescence, photosynthesis, and photochemistry.[14,37,38,40–42,45,51,52,59,70–72,86,89–92] In this case, a necessary and essential step is to test with model systems of a similar kind when the exact result can be known. The benchmark study would provide practical guidance in simulations of realistic nonadiabatic processes in complex condensed phases, such as organic photovoltaics, luminescence, photosynthesis, and photochemistry.

11 July 2024 19:27:18

SUPPLEMENTARY MATERIAL

See the supplementary material for the discretization of the spectral density, the LVC model parameters, the population and coherence dynamics as well as the root mean square error (RMSE) of spin-boson models No. 1–9 at different temperatures, ground state population dynamics of retinal with focused sampling methods, Tully's SAC and DAC models with different initial momenta, LCP model results, computational cost of approximate dynamics, as well as the previous works on relevant models. The numerically exact results of the tested models are available at https://github.com/xiangsunlab/benchmark-data.

AUTHOR DECLARATIONS

Conflict of Interest

The authors have no conflicts to disclose.

Author Contributions

Z. L. and N. L. contributed equally to this work.

Zengkui Liu: Data curation (lead); Formal analysis (equal); Investigation (equal); Methodology (equal); Software (equal); Writing – original draft (equal). **Ningyi Lyu**: Data curation (lead); Formal analysis (equal); Investigation (equal); Methodology (equal); Software (equal); Writing – original draft (equal). **Zhubin Hu**: Methodology (equal); Software (equal). **Hao Zeng**: Data curation (equal); Validation (equal). **Victor S. Batista**: Funding acquisition (equal); Methodology (equal); Writing – review & editing (equal). **Xiang Sun**: Conceptualization (lead); Formal analysis (equal); Funding acquisition (lead); Methodology (equal); Software (equal); Supervision (lead); Writing – review & editing (lead).

DATA AVAILABILITY

The data that support the findings of this study are available from the corresponding author upon reasonable request.

REFERENCES

[1] A. Nitzan, *Chemical Dynamics in Condensed Phases: Relaxation, Transfer and Reactions in Condensed Molecular Systems* (Oxford University Press, New York, 2006).

[2] W. H. Miller, "The semiclassical initial value representation: A potentially practical way for adding quantum effects to classical molecular dynamics simulations," J. Phys. Chem. A **105**, 2942–2955 (2001).

[3] S. M. Greene and V. S. Batista, "Tensor-train split-operator Fourier transform (TT-SOFT) method: Multidimensional nonadiabatic quantum dynamics," J. Chem. Theory Comput. **13**, 4034–4042 (2017).

[4] E. Mulvihill, A. Schubert, X. Sun, B. D. Dunietz, and E. Geva, "A modified approach for simulating electronically nonadiabatic dynamics via the generalized quantum master equation," J. Chem. Phys. **150**, 034101 (2019).

[5] E. Mulvihill, X. Gao, Y. Liu, A. Schubert, B. D. Dunietz, and E. Geva, "Combining the mapping Hamiltonian linearized semiclassical approach with the generalized quantum master equation to simulate electronically nonadiabatic molecular dynamics," J. Chem. Phys. **151**, 074103 (2019).

[6] X. Sun and E. Geva, "Equilibrium Fermi's golden rule charge transfer rate constants in the condensed phase: The linearized semiclassical method vs classical Marcus theory," J. Phys. Chem. A **120**, 2976–2990 (2016).

[7] X. Sun and E. Geva, "Nonequilibrium Fermi's golden rule charge transfer rates via the linearized semiclassical method," J. Chem. Theory Comput. **12**, 2926–2941 (2016).

[8] X. Sun, P. Zhang, Y. Lai, K. L. Williams, M. S. Cheung, B. D. Dunietz, and E. Geva, "Computational study of charge-transfer dynamics in the carotenoid–porphyrin–C_{60} molecular triad solvated in explicit tetrahydrofuran and its spectroscopic signature," J. Phys. Chem. C **122**, 11288–11299 (2018).

[9] Z. Tong, X. Gao, M. S. Cheung, B. D. Dunietz, E. Geva, and X. Sun, "Charge transfer rate constants for the carotenoid–porphyrin–C_{60} molecular triad dissolved in tetrahydrofuran: The spin-boson model vs the linearized semiclassical approximation," J. Chem. Phys. **153**, 044105 (2020).

[10] Z. Hu, Z. Tong, M. S. Cheung, B. D. Dunietz, E. Geva, and X. Sun, "Photoinduced charge transfer dynamics in the carotenoid–porphyrin–C_{60} triad via the linearized semiclassical nonequilibrium Fermi's golden rule," J. Phys. Chem. B **124**, 9579–9591 (2020).

[11] V. May and O. Kühn, *Charge and Energy Transfer Dynamics in Molecular Systems* (Wiley, Weinheim, 2011).

[12] S. J. Jang, *Dynamics of Molecular Excitons: Theories and Applications* (Elsevier, Amsterdam, 2020).

[13] A. Ishizaki and G. R. Fleming, "Theoretical examination of quantum coherence in a photosynthetic system at physiological temperature," Proc. Natl. Acad. Sci. U.S.A. **106**, 17255–17260 (2009).

[14] Z. Hu and X. Sun, "All-atom nonadiabatic semiclassical mapping dynamics for photoinduced charge transfer of organic photovoltaic molecules in explicit solvents," J. Chem. Theory Comput. **18**, 5819–5836 (2022).

[15] J.-J. Yang, X.-Y. Liu, Z.-W. Li, T. Frauenheim, C. Yam, W.-H. Fang, and G. Cui, "The spin–orbit interaction controls photoinduced interfacial electron transfer in fullerene–perovskite heterojunctions: C_{60} versus C_{70}," Phys. Chem. Chem. Phys. **23**, 6536–6543 (2021).

[16] L. Qiao, W.-H. Fang, R. Long, and O. V. Prezhdo, "Photoinduced dynamics of charge carriers in metal halide perovskites from an atomistic perspective," J. Phys. Chem. Lett. **11**, 7066–7082 (2020).

[17] J. Z. H. Zhang, *Theory and Application of Quantum Molecular Dynamics* (World Scientific, Singapore, 1999).

[18] D. T. Colbert and W. H. Miller, "A novel discrete variable representation for quantum mechanical reactive scattering via the S-matrix Kohn method," J. Chem. Phys. **96**, 1982–1991 (1992).

[19] X. Chen and V. S. Batista, "Matching-pursuit/split-operator-Fourier-transform simulations of excited-state nonadiabatic quantum dynamics in pyrazine," J. Chem. Phys. **125**, 124313 (2006).

[20] N. Lyu, M. B. Soley, and V. S. Batista, "Tensor-train split-operator KSL (TT-SOKSL) method for quantum dynamics simulations," J. Chem. Theory Comput. **18**, 3327–3346 (2022).

[21] Y. Tanimura and R. Kubo, "Time evolution of a quantum system in contact with a nearly Gaussian-Markoffian noise bath," J. Phys. Soc. Jpn. **58**, 101–114 (1989).

[22] Y. Tanimura, "Numerically "exact" approach to open quantum dynamics: The hierarchical equations of motion (HEOM)," J. Chem. Phys. **153**, 020901 (2020).

[23] J. Ren, Z. Shuai, and G. Kin-Lic Chan, "Time-dependent density matrix renormalization group algorithms for nearly exact absorption and fluorescence spectra of molecular aggregates at both zero and finite temperature," J. Chem. Theory Comput. **14**, 5027–5039 (2018).

[24] A. Baiardi and M. Reiher, "Large-scale quantum dynamics with matrix product states," J. Chem. Theory Comput. **15**, 3481–3498 (2019).

[25] W. Li, J. Ren, and Z. Shuai, "Numerical assessment for accuracy and GPU acceleration of TD-DMRG time evolution schemes," J. Chem. Phys. **152**, 024127 (2020).

[26] N. Makri and D. E. Makarov, "Tensor propagator for iterative quantum time evolution of reduced density matrices. I. Theory," J. Chem. Phys. **102**, 4600–4610 (1995).

[27] N. Makri and D. E. Makarov, "Tensor propagator for iterative quantum time evolution of reduced density matrices. II. Numerical methodology," J. Chem. Phys. **102**, 4611–4618 (1995).

[28] N. Makri and K. Thompson, "Semiclassical influence functionals for quantum systems in anharmonic environments," Chem. Phys. Lett. **291**, 101–109 (1998).

[29] N. Makri, "The linear response approximation and its lowest order corrections: An influence functional approach," J. Phys. Chem. B **103**, 2823–2829 (1999).

[30] J. Shao and N. Makri, "Influence functional from a bath of coupled time-dependent harmonic oscillators," Phys. Rev. E **59**, 269–274 (1999).

[31] Y. Tanimura and S. Mukamel, "Two-dimensional femtosecond vibrational spectroscopy of liquids," J. Chem. Phys. **99**, 9496–9511 (1993).

[32] W. H. Miller, "Semiclassical theory of atom-diatom collisions: Path integrals and the classical S matrix," J. Chem. Phys. **53**, 1949–1959 (1970).

[33] H. D. Meyer and W. H. Miller, "A classical analog for electronic degrees of freedom in nonadiabatic collision processes," J. Chem. Phys. **70**, 3214–3223 (1979).

[34] G. Stock and M. Thoss, "Semiclassical description of nonadiabatic quantum dynamics," Phys. Rev. Lett. **78**, 578–581 (1997).

[35] H. Wang, X. Sun, and W. H. Miller, "Semiclassical approximations for the calculation of thermal rate constants for chemical reactions in complex molecular systems," J. Chem. Phys. **108**, 9726–9736 (1998).

[36] E. A. Coronado, J. Xing, and W. H. Miller, "Ultrafast non-adiabatic dynamics of systems with multiple surface crossings: A test of the Meyer-Miller Hamiltonian with semiclassical initial value representation methods," Chem. Phys. Lett. **349**, 521–529 (2001).

[37] S. J. Cotton and W. H. Miller, "Symmetrical windowing for quantum states in quasi-classical trajectory simulations: Application to electronically non-adiabatic processes," J. Chem. Phys. **139**, 234112 (2013).

[38] S. J. Cotton and W. H. Miller, "A new symmetrical quasi-classical model for electronically non-adiabatic processes: Application to the case of weak non-adiabatic coupling," J. Chem. Phys. **145**, 144108 (2016).

[39] X. He and J. Liu, "A new perspective for nonadiabatic dynamics with phase space mapping models," J. Chem. Phys. **151**, 024105 (2019).

[40] J. E. Runeson and J. O. Richardson, "Spin-mapping approach for nonadiabatic molecular dynamics," J. Chem. Phys. **151**, 044119 (2019).

[41] J. E. Runeson and J. O. Richardson, "Generalized spin mapping for quantum-classical dynamics," J. Chem. Phys. **152**, 084110 (2020).

[42] M. A. C. Saller, A. Kelly, and J. O. Richardson, "On the identity of the identity operator in nonadiabatic linearized semiclassical dynamics," J. Chem. Phys. **150**, 071101 (2019).

[43] J. Schwinger, *Quantum Theory of Angular Momentum: A Collection of Reprints and Original Papers* (Academic Press, New York, 1965).

[44] M. Thoss and G. Stock, "Mapping approach to the semiclassical description of nonadiabatic quantum dynamics," Phys. Rev. A **59**, 64–79 (1999).

[45] X. Sun, H. Wang, and W. H. Miller, "Semiclassical theory of electronically nonadiabatic dynamics: Results of a linearized approximation to the initial value representation," J. Chem. Phys. **109**, 7064–7074 (1998).

[46] Q. Shi and E. Geva, "Nonradiative electronic relaxation rate constants from approximations based on linearizing the path-integral forward–backward action," J. Phys. Chem. A **108**, 6109–6116 (2004).

[47] J. A. Poulsen, G. Nyman, and P. J. Rossky, "Practical evaluation of condensed phase quantum correlation functions: A Feynman-Kleinert variational linearized path integral method," J. Chem. Phys. **119**, 12179–12193 (2003).

[48] J. A. Poulsen, G. Nyman, and P. J. Rossky, "Quantum diffusion in liquid para-hydrogen: An application of the Feynman–Kleinert linearized path integral approximation," J. Phys. Chem. B **108**, 19799–19808 (2004).

[49] J. A. Poulsen, G. Nyman, and P. J. Rossky, "Determination of the van hove spectrum of liquid He(4): An application of the Feynman–Kleinert linearized path integral methodology," J. Phys. Chem. A **108**, 8743–8751 (2004).

[50] B. J. Ka, Q. Shi, and E. Geva, "Vibrational energy relaxation rates via the linearized semiclassical approximation: Applications to neat diatomic liquids and atomic–diatomic liquid mixtures," J. Phys. Chem. A **109**, 5527–5536 (2005).

[51] H. Kim, A. Nassimi, and R. Kapral, "Quantum-classical Liouville dynamics in the mapping basis," J. Chem. Phys. **129**, 084102 (2008).

[52] X. Gao, M. A. C. Saller, Y. Liu, A. Kelly, J. O. Richardson, and E. Geva, "Benchmarking quasiclassical mapping Hamiltonian methods for simulating electronically nonadiabatic molecular dynamics," J. Chem. Theory Comput. **16**, 2883–2895 (2020).

[53] W. H. Miller and S. J. Cotton, "Communication: Wigner functions in action-angle variables, Bohr-Sommerfeld quantization, the Heisenberg correspondence principle, and a symmetrical quasi-classical approach to the full electronic density matrix," J. Chem. Phys. **145**, 081102 (2016).

[54] S. J. Cotton and W. H. Miller, "Trajectory-adjusted electronic zero point energy in classical Meyer-Miller vibronic dynamics: Symmetrical quasiclassical application to photodissociation," J. Chem. Phys. **150**, 194110 (2019).

[55] S. J. Cotton and W. H. Miller, "A symmetrical quasi-classical spin-mapping model for the electronic degrees of freedom in non-adiabatic processes," J. Phys. Chem. A **119**, 12138–12145 (2015).

[56] H.-D. Meyer and W. H. Miller, "Classical models for electronic degrees of freedom: Derivation via spin analogy and application to F^* + H_2 → F + H_2," J. Chem. Phys. **71**, 2156–2169 (1979).

[57] D. Bossion, W. Ying, S. N. Chowdhury, and P. Huo, "Non-adiabatic mapping dynamics in the phase space of the $SU(N)$ lie group," J. Chem. Phys. **157**, 084105 (2022).

[58] T. Tilma and K. Nemoto, "$SU(N)$-Symmetric quasi-probability distribution functions," J. Phys. A: Math. Theor. **45**, 015302 (2012).

[59] X. He, Z. Gong, B. Wu, and J. Liu, "Negative zero-point-energy parameter in the Meyer-Miller mapping model for nonadiabatic dynamics," J. Phys. Chem. Lett. **12**, 2496–2501 (2021).

[60] J. Liu, X. He, and B. Wu, "Unified formulation of phase space mapping approaches for nonadiabatic quantum dynamics," Acc. Chem. Res. **54**, 4215–4228 (2021).

[61] S. Bonella and D. F. Coker, "Semiclassical implementation of the mapping Hamiltonian approach for nonadiabatic dynamics using focused initial distribution sampling," J. Chem. Phys. **118**, 4370–4385 (2003).

[62] J. Liu, "A unified theoretical framework for mapping models for the multi-state Hamiltonian," J. Chem. Phys. **145**, 204105 (2016).

[63] C. Lubich, I. V. Oseledets, and B. Vandereycken, "Time integration of tensor trains," SIAM J. Numer. Anal. **53**, 917–941 (2015).

[64] J. Haegeman, C. Lubich, I. Oseledets, B. Vandereycken, and F. Verstraete, "Unifying time evolution and optimization with matrix product states," Phys. Rev. B **94**, 165116 (2016).

[65] X. Xie, Y. Liu, Y. Yao, U. Schollwöck, C. Liu, and H. Ma, "Time-dependent density matrix renormalization group quantum dynamics for realistic chemical systems," J. Chem. Phys. **151**, 224101 (2019).

[66] J. Ren, W. Li, T. Jiang, Y. Wang, and Z. Shuai, "Time-dependent density matrix renormalization group method for quantum dynamics in complex systems," Wiley Interdisc. Rev.: Comput. Mol. Sci. **12**, e1614 (2022).

[67] R. Borrelli and M. F. Gelin, "Quantum electron-vibrational dynamics at finite temperature: Thermo field dynamics approach," J. Chem. Phys. **145**, 224101 (2016).

[68] R. Borrelli and M. F. Gelin, "Finite temperature quantum dynamics of complex systems: Integrating thermo-field theories and tensor-train methods," Wiley Interdisc. Rev.: Comput. Mol. Sci. **11**, e1539 (2021).

[69] N. Lyu, E. Mulvihill, M. B. Soley, E. Geva, and V. S. Batista, "Tensor-train thermo-field memory kernels for generalized quantum master equations," J. Chem. Theory Comput. **19**, 1111–1129 (2023).

[70] S. J. Cotton, K. Igumenshchev, and W. H. Miller, "Symmetrical windowing for quantum states in quasi-classical trajectory simulations: Application to electron transfer," J. Chem. Phys. **141**, 084104 (2014).

[71] Z. Hu, D. Brian, and X. Sun, "Multi-state harmonic models with globally shared bath for nonadiabatic dynamics in the condensed phase," J. Chem. Phys. **155**, 124105 (2021).

[72] L. E. Cook, J. E. Runeson, J. O. Richardson, and T. J. H. Hele, "Which algorithm best propagates the Meyer–Miller–Stock–Thoss mapping Hamiltonian for nonadiabatic dynamics?," J. Chem. Theory Comput. **19**, 6109–6125 (2023).

11 July 2024 19:27:18

[73]M. S. Church, T. J. H. Hele, G. S. Ezra, and N. Ananth, "Nonadiabatic semi-classical dynamics in the mixed quantum-classical initial value representation," J. Chem. Phys. **148**, 102326 (2018).

[74]J. O. Richardson, P. Meyer, M.-O. Pleinert, and M. Thoss, "An analysis of nonadiabatic ring-polymer molecular dynamics and its application to vibronic spectra," Chem. Phys. **482**, 124–134 (2017).

[75]X. He, B. Wu, Y. Shang, B. Li, X. Cheng, and J. Liu, "New phase space formulations and quantum dynamics approaches," Wiley Interdiscip. Rev.: Comput. Mol. Sci. **12**, e1619 (2022).

[76]Q. Shi and E. Geva, "Vibrational energy relaxation in liquid oxygen from a semiclassical molecular dynamics simulation," J. Phys. Chem. A **107**, 9070–9078 (2003).

[77]Q. Shi and E. Geva, "Vibrational energy relaxation rate constants from linear response theory," J. Chem. Phys. **118**, 7562 (2003).

[78]Q. Shi and E. Geva, "A derivation of the mixed quantum-classical Liouville equation from the influence functional formalism," J. Chem. Phys. **121**, 3393–3404 (2004).

[79]Q. Shi and E. Geva, "A semiclassical generalized quantum master equation for an arbitrary system-bath coupling," J. Chem. Phys. **120**, 10647 (2004).

[80]Q. Shi and E. Geva, "A comparison between different semiclassical approximations for optical response functions in nonpolar liquid solutions," J. Chem. Phys. **122**, 064506 (2005).

[81]Q. Shi and E. Geva, "A comparison between different semiclassical approximations for optical response functions in nonpolar liquid solution. II. The signature of excited state dynamics on two-dimensional spectra," J. Chem. Phys. **129**, 124505 (2008).

[82]B. J. Ka and E. Geva, "Vibrational energy relaxation of polyatomic molecules in liquid solution via the linearized semiclassical method," J. Phys. Chem. A **110**, 9555–9567 (2006).

[83]F. X. Vázquez, I. Navrotskaya, and E. Geva, "Vibrational energy relaxation rates via the linearized semiclassical method without force derivatives," J. Phys. Chem. A **114**, 5682–5688 (2010).

[84]F. X. Vázquez, S. Talapatra, and E. Geva, "Vibrational energy relaxation in liquid HCl and DCl via the linearized semiclassical method: Electrostriction versus quantum delocalization," J. Phys. Chem. A **115**, 9775–9781 (2011).

[85]P. L. McRobbie and E. Geva, "A benchmark study of different methods for calculating one- and two-dimensional optical spectra," J. Phys. Chem. A **113**, 10425–10434 (2009).

[86]M. A. C. Saller, A. Kelly, and J. O. Richardson, "Improved population operators for multi-state nonadiabatic dynamics with the mixed quantum-classical mapping approach," Faraday Discuss. **221**, 150–167 (2020).

[87]X. Gao and E. Geva, "A nonperturbative methodology for simulating multidimensional spectra of multiexcitonic molecular systems via quasiclassical mapping Hamiltonian methods," J. Chem. Theory Comput. **16**, 6491–6502 (2020).

[88]X. Gao, Y. Lai, and E. Geva, "Simulating absorption spectra of multiexcitonic systems via quasiclassical mapping Hamiltonian methods," J. Chem. Theory Comput. **16**, 6465–6480 (2020).

[89]Y. Liu, X. Gao, Y. Lai, E. Mulvihill, and E. Geva, "Electronic dynamics through conical intersections via quasiclassical mapping Hamiltonian methods," J. Chem. Theory Comput. **16**, 4479–4488 (2020).

[90]M. A. C. Saller, A. Kelly, and E. Geva, "Benchmarking quasiclassical mapping Hamiltonian methods for simulating cavity-modified molecular dynamics," J. Phys. Chem. Lett. **12**, 3163–3170 (2021).

[91]S. J. Cotton, R. Liang, and W. H. Miller, "On the adiabatic representation of Meyer-Miller electronic-nuclear dynamics," J. Chem. Phys. **147**, 064112 (2017).

[92]S. J. Cotton and W. H. Miller, "A symmetrical quasi-classical windowing model for the molecular dynamics treatment of non-adiabatic processes involving many electronic states," J. Chem. Phys. **150**, 104101 (2019).

[93]K. Miyazaki and N. Ananth, "Nonadiabatic simulations of photoisomerization and dissociation in ethylene using *ab initio* classical trajectories," J. Chem. Phys. **159**, 124110 (2023).

[94]P. Ehrenfest, "Comment on the approximate validity of classical mechanics within quantum mechanics," Z. Phys. **45**, 455–457 (1927).

[95]A. D. McLachlan, "A variational solution of the time-dependent Schrodinger equation," Mol. Phys. **8**, 39–44 (1964).

[96]R. Crespo-Otero and M. Barbatti, "Recent advances and perspectives on nonadiabatic mixed quantum–classical dynamics," Chem. Rev. **118**, 7026–7068 (2018).

[97]D. Xu and K. Schulten, "Coupling of protein motion to electron transfer in a photosynthetic reaction center: Investigating the low temperature behavior in the framework of the spin-boson model," Chem. Phys. **182**, 91–117 (1994).

[98]J. Adolphs and T. Renger, "How proteins trigger excitation energy transfer in the FMO complex of green sulfur bacteria," Biophys. J. **91**, 2778–2797 (2006).

[99]A. Ishizaki and G. R. Fleming, "Quantum coherence in photosynthetic light harvesting," Annu. Rev. Condens. Matter Phys. **3**, 333–361 (2012).

[100]X. Sun and E. Geva, "Exact vs. asymptotic spectral densities in the Garg-Onuchic-Ambegaokar charge transfer model and its effect on Fermi's golden rule rate constants," J. Chem. Phys. **144**, 044106 (2016).

[101]P. L. Walters, T. C. Allen, and N. Makri, "Direct determination of discrete harmonic bath parameters from molecular dynamics simulations," J. Comput. Chem. **38**, 110–115 (2017).

[102]M. D. Newton and N. Sutin, "Electron transfer reactions in condensed phases," Annu. Rev. Phys. Chem. **35**, 437–480 (1984).

[103]E. Mulvihill and E. Geva, "A road map to various pathways for calculating the memory kernel of the generalized quantum master equation," J. Phys. Chem. B **125**, 9834–9852 (2021).

[104]Z. Tang, X. Ouyang, Z. Gong, H. Wang, and J. Wu, "Extended hierarchy equation of motion for the spin-boson model," J. Chem. Phys. **143**, 224112 (2015).

[105]A. F. Izmaylov, D. Mendive Tapia, M. J. Bearpark, M. A. Robb, J. C. Tully, and M. J. Frisch, "Nonequilibrium Fermi golden rule for electronic transitions through conical intersections," J. Chem. Phys. **135**, 234106 (2011).

[106]S. Hahn and G. Stock, "Femtosecond secondary emission arising from the nonadiabatic photoisomerization in rhodopsin," Chem. Phys. **259**, 297–312 (2000).

[107]J. C. Tully, "Molecular dynamics with electronic transitions," J. Chem. Phys. **93**, 1061–1071 (1990).

[108]O. V. Prezhdo and P. J. Rossky, "Mean-field molecular dynamics with surface hopping," J. Chem. Phys. **107**, 825–834 (1997).

[109]A. Kelly, N. Brackbill, and T. E. Markland, "Accurate nonadiabatic quantum dynamics on the cheap: Making the most of mean field theory with master equations," J. Chem. Phys. **142**, 094110 (2015).

[110]X. Guo, J. Xu, G. Li, and L. Wang, "Interpretation of adiabatic and diabatic populations from trajectories of branching corrected surface hopping," Chin. J. Chem. Phys. **35**, 488–498 (2022).

[111]P. Huo and D. F. Coker, "Communication: Partial linearized density matrix dynamics for dissipative, non-adiabatic quantum evolution," J. Chem. Phys. **135**, 201101 (2011).

[112]P. Huo and D. F. Coker, "Semi-classical path integral non-adiabatic dynamics: A partial linearized classical mapping Hamiltonian approach," Mol. Phys. **110**, 1035–1052 (2012).

[113]J. R. Mannouch and J. O. Richardson, "A partially linearized spin-mapping approach for nonadiabatic dynamics. I. Derivation of the theory," J. Chem. Phys. **153**, 194109 (2020).

[114]J. R. Mannouch and J. O. Richardson, "A partially linearized spin-mapping approach for nonadiabatic dynamics. II. Analysis and comparison with related approaches," J. Chem. Phys. **153**, 194110 (2020).

[115]Z. Liu, H. Hu, and X. Sun, "Multistate reaction coordinate model for charge and energy transfer dynamics in the condensed phase," J. Chem. Theory Comput. **19**, 7151–7170 (2023).

[116]X. Sun, X. Zhang, and Z. Liu, "Generalized nonequilibrium Fermi's golden rule and its semiclassical approximations for electronic transitions between multiple states," J. Chem. Phys. **160**, 034108 (2024).

[117]Z. Liu, Z. Song, and X. Sun, "All-atom photoinduced charge transfer dynamics in condensed phase via multistate nonlinear-response instantaneous Marcus theory," J. Chem. Theory Comput. **20**, 3993–4006 (2024).

[118]X. Sun and Z. Liu, "Semiclassical approaches to perturbative time-convolution and time-convolutionless quantum master equations for electronic transitions in multistate systems," J. Chem. Phys. **160**, 174113 (2024).

[119]X. He, B. Wu, Z. Gong, and J. Liu, "Commutator matrix in phase space mapping models for nonadiabatic quantum dynamics," J. Phys. Chem. A **125**, 6845–6863 (2021).

11 July 2024 19:27:18